

1 **Assessment and Applications of NASA Ozone Data Products**
2 **Derived from Aura OMI/MLS Satellite Measurements in Context of**
3 **the GMI Chemical Transport Model**

4
5
6 Ziemke^{1,2}, J. R., M. A. Olsen^{1,2}, J. C. Witte³, A. R. Douglass², S. E. Strahan^{2,4}, K. Wargan^{2,3}, X.
7 Liu⁵, M. R. Schoeberl⁶, K Yang⁷, T. B. Kaplan⁸, S. Pawson², B. N. Duncan², P. A. Newman², P.
8 K. Bhartia², M. K. Heney³

9 ¹Morgan State University, Baltimore, Maryland, USA

10 ²NASA Goddard Space Flight Center, Greenbelt, Maryland, USA

11 ³Science Systems and Applications Inc., Lanham, Maryland, USA

12 ⁴Universities Space Research Association, Columbia, Maryland, USA

13 ⁵Harvard-Smithsonian Center for Astrophysics, Cambridge, Massachusetts, USA

14 ⁶Science and Technology Corporation, Lanham, Maryland, USA

15 ⁷University of Maryland College Park, Maryland, USA

16 ⁸INNOVIM, Greenbelt, Maryland, USA

17 *(Submitted to Journal of Geophysical Research Atmospheres, 19 September, 2013)*

18
19 **Abstract.** Measurements from the Ozone Monitoring Instrument (OMI) and Microwave Limb
20 Sounder (MLS), both onboard the Aura spacecraft, have been used to produce daily global maps
21 of column and profile ozone since August 2004. Here we compare and evaluate three strategies

22 to obtain daily maps of tropospheric and stratospheric ozone from OMI and MLS measurements:
23 trajectory mapping, direct profile retrieval, and data assimilation. Evaluation is based upon an
24 assessment that includes validation using ozonesondes and comparisons with the Global
25 Modeling Initiative (GMI) chemical transport model (CTM). We investigate applications of the
26 three ozone data products from near-decadal and inter-annual timescales to day-to-day case
27 studies. Zonally averaged inter-annual changes in tropospheric ozone from all of the products in
28 any latitude range are of the order 1-2 Dobson Units while changes (increases) over the 8-year
29 Aura record investigated <http://eosps0.gsfc.nasa.gov/atbd-category/49> vary ~2-4 Dobson Units.
30 It is demonstrated that all of the ozone products can measure and monitor exceptional
31 tropospheric ozone events including major forest fire and pollution transport events.
32 Stratospheric ozone during the Aura record has several anomalous inter-annual events including
33 stratospheric warming split events in the Northern Hemisphere extra-tropics that are well
34 captured using the data assimilation ozone profile product. Data assimilation with continuous
35 daily global coverage and vertical ozone profile information is the best of the three strategies at
36 generating a global tropospheric and stratospheric ozone product for science applications.

37

38 **1. Introduction.**

39

40 Subtraction of stratospheric column ozone (SCO) from total ozone column, known as the
41 tropospheric ozone residual method, yields a quantitative measure of tropospheric column ozone
42 (TCO) from satellite remote sensing [*Fishman and Larsen, 1987; 1990*]. The original
43 application of the method subtracted SCO obtained from Stratospheric Aerosol and Gas
44 Experiment (SAGE) profiles from co-located Total Ozone Mapping Spectrometer (TOMS) total

45 column ozone. This residual concept has also been used with TOMS total ozone and SCO from
46 Solar Backscatter Ultraviolet (SBUV) instruments [*Fishman et al.*, 2003] and from the Upper
47 Atmosphere Research Satellite Microwave Limb Sounder (MLS) instrument [*Chandra et al.*,
48 2003]. Other methods to derive TCO from satellite measurements include a modified residual
49 method incorporating TOMS-only total ozone [*Hudson and Thompson*, 1998], a UV radiance
50 scan-angle method [*Kim, et al.*, 2001], a topography differencing method [*Newchurch et al.*,
51 2001], and cloud slicing using deep convective clouds [*Ziemke et al.*, 1998, 2009]. These
52 techniques produce tropospheric ozone fields that have limited temporal or spatial coverage.

53
54 Our study focuses on ozone measurements from two Aura instruments, the Ozone Monitoring
55 Instrument (OMI) and the Microwave Limb Sounder (MLS). These two instruments are
56 currently operating and their measurements are being used in several new algorithms for deriving
57 tropospheric and stratospheric ozone, both in column amounts and profiles. While the MLS
58 instrument remains fully functional for measuring ozone and other trace gases, the OMI
59 measurements are impacted by a “row anomaly” artifact which became large in January 2009
60 adversely affecting more than one third of the ozone measurements. *Liu et al.* [2010a, 2010b]
61 uses an optimal estimation technique to determine ozone profiles from OMI radiances. This is a
62 direct profile retrieval method using a single instrument and gives both stratospheric and
63 tropospheric column ozone once the tropopause is specified. Although ozone profile retrievals
64 are possible over the entire OMI record using this technique, the row anomaly adversely affected
65 profiles after January 2009 (our study uses only ozone profiles through December 2008.) We
66 also evaluate fields produced by data assimilation of OMI and MLS ozone measurements
67 [*Wargan et al.*, 2013]. The third product investigated uses a trajectory mapping technique

68 [Schoeberl *et al.*, 2007] that estimates SCO fields by advecting MLS profile ozone from wind
69 analyses and filling in subsequent SCO measurements between MLS orbits. TCO then follows
70 from the trajectory mapping method by subtracting SCO from OMI total column ozone.
71 Schoeberl *et al.* [2007] discuss improvements in daily TCO and SCO measurements from the
72 OMI/MLS 2D Gaussian/linear interpolation method of Ziemke *et al.* [2006]. The assimilation
73 and trajectory techniques both invoke MLS measurements that have better profile resolution near
74 the tropopause for separating tropospheric from stratospheric column ozone compared to direct
75 nadir profile retrieval.

76

77 The purpose of our study is to assess data quality and science application capability of these
78 three gridded OMI/MLS ozone products. Assessment of the products includes comparisons with
79 ozonesondes and ozone simulated using the Global Modeling Initiative (GMI) chemistry and
80 transport model (CTM) as well as evaluation of the suitability of these products for science
81 applications. The following sections 2 and 3 describe the datasets used and the GMI CTM.
82 Section 4 provides a brief description of the three ozone data products evaluated in our study.
83 Section 5 shows ozonesonde comparisons for validation of the products while section 6 discusses
84 fundamental seasonal and spatial characteristics for these products. Section 7 describes
85 applications for the products and finally section 8 provides a summary.

86

87 **2. Description of relevant data sets.**

88

89 Ozone data from Aura OMI and MLS instruments are used to create daily maps of tropospheric
90 column ozone (TCO) and profile ozone. The OMI and MLS ozone data have been archived as

91 level-2 (along-orbit swath) and level-3 (gridded for OMI) beginning in late August 2004. The
92 Aura OMI is a nadir-scanning instrument. At visible and UV wavelengths OMI detects
93 backscattered solar radiance to measure daytime total column ozone over the Earth with a
94 resolution of 13 km × 24 km at absolute nadir. Documentation for the OMI instrument and data
95 may be obtained from the webpage <http://eosps0.gsfc.nasa.gov/atbd-category/49>. Our analyses
96 use OMI version 8.5 ozone measurements which include several changes from version 8
97 including measured cloud pressures [*Vasilkov et al.*, 2008]. The sensitivity of OMTO3 to ozone
98 varies from region to region (due to changes in surface reflectivity) and strongly with altitude,
99 especially in the troposphere where retrieval efficiency on average varies from ~100% in the
100 stratosphere and upper troposphere to 40-70% at 3 km. The use of OMI spectra in the direct
101 ozone profile retrieval slightly increases the retrieval efficiency in the lower troposphere [*Liu et*
102 *al.*, 2010a].

103
104 The Aura MLS instrument measures vertical profiles of ozone tangent to the Earth's surface in
105 the stratosphere and upper troposphere along the Aura orbital track beginning about 7 minutes
106 before OMI for ascending orbit daytime measurements from MLS. This measurement time
107 difference occurs because MLS looks forward along orbital path while OMI looks down.
108 Because MLS detects microwave emission, this instrument measures ozone profiles during both
109 daytime (ascending orbit) and nighttime (descending orbit). All of the ozone products which use
110 MLS data include both day and night v3.3 measurements. Data quality and description of the
111 MLS version 3.3 ozone profile product are discussed by *Livesey et al.* [2011].

112

113 Ozonesonde measurements are used for validation of the tropospheric ozone data products. This
114 validation includes ozonesonde profile measurements from the World Ozone and Ultraviolet
115 Radiation Data Centre (WOUDC), Southern Hemisphere Additional OZonesondes (SHADOZ),
116 and Network for the Detection of Atmospheric Composition Change (NDACC). For consistency
117 the tropopause pressure obtained from the NCEP 2K-km⁻¹ vertical lapse rate definition is applied
118 for determining TCO and SCO for all of the products including ozonesondes.

119

120 **3. Description of the GMI model.**

121

122 The GMI CTM includes a photochemical mechanism appropriate for the stratosphere and
123 troposphere and is described by *Duncan et al.* [2007] and *Strahan et al.* [2007]. The emissions
124 of trace gases and the aerosol fields used in the simulations are described by *Duncan et al.*
125 [2008], except for the biomass burning emissions that are described by *van der Werf et al.*
126 [2006]. The emission sources include industry/fossil fuel, biomass burning, biofuel
127 combustions, and contributions from aircraft. The global emissions for year 2004 through year
128 2008 for the CTM are observationally derived daily emissions. Global emissions in the model
129 for year 2008 are repeated for each of the following years 2009-2012. The meteorological input
130 fields for the model are from Modern Era Retrospective analysis for Research and Applications
131 (MERRA).

132

133 **4. Description of the ozone data products.**

134

135 4.1. Trajectory mapping.

136

137 *Schoeberl et al.* [2007] describe a wind trajectory algorithm for producing high horizontal
138 resolution maps of stratospheric and tropospheric column ozone. With this method the along-
139 track profile v3.3 ozone from MLS each day is advected 2-days forward and 2-days backward to
140 produce fields of stratospheric ozone profiles. These daily ozone profiles are then vertically
141 integrated to produce high resolution ($1^{\circ} \times 1.25^{\circ}$) gridded maps of SCO. The gridded SCO is then
142 subtracted from coincident total column ozone from OMI to produce daily global maps of TCO.
143 This method produces daily global maps that include regions associated with the dynamical wind
144 jets. Vertical resolution from MLS is ~ 3 km about the tropopause for separating ozone in the
145 troposphere and stratosphere. The speed for the trajectory algorithm is fast when compared to
146 direct profile retrieval (section 4.2) or data assimilation methods (section 4.3). The fields
147 produced using this method incorporate MERRA assimilated winds, the same winds as used by
148 the GMI CTM described in section 3. The current version of the trajectory mapping product
149 includes an improved tropopause pressure definition, corrects for a time stamp error which
150 affected daily time iteration steps, and flags out bad retrieval measurements for high resolution
151 mode days (occurring one day out of every 32 days). We have improved the trajectory mapping
152 product on several points from the original product of *Schoeberl et al.* [2007].

153

154 4.2. Nadir profile.

155

156 In the OMI ozone profile algorithm the profile of partial ozone columns in Dobson Unit (DU) is
157 retrieved at 24 layers from the surface to ~ 60 km (~ 2.5 -km thick per layer) from BUUV radiances
158 in the spectral region 270-330 nm using the optimal estimation technique [*Liu et al.*, 2010a,

159 2010b]. This retrieval scheme approaches an optimal solution by simultaneously and iteratively
160 minimizing the differences between measured and simulated radiances and between retrieved
161 and *a priori* state vectors, constrained by measurement error and the monthly and zonally mean
162 LLM ozone profile climatology [McPeters *et al.*, 2007]. The retrieved ozone profiles have 4 to 7
163 layers in the troposphere, depending on the latitude. The horizontal resolution of our retrievals
164 used here is 52x48 km² at nadir by co-adding 4 UV1 (8 UV2) pixels. The vertical resolution,
165 estimated by Liu *et al.* [2010a], varies from 7-11 km in the troposphere and 10-14 km in the
166 stratosphere. The retrieval errors (defined as the root sum square of precisions and smoothing
167 errors) range from 1-6 % in the stratosphere to 6-35 % in the troposphere. The retrieval errors in
168 tropospheric ozone columns are typically within 2-4 DU. For this study we use the daily data
169 gridded to 2.5° longitude × 2° latitude. As the retrieval quality degrades due to the occurrence of
170 OMI row anomaly, only retrievals from October 2004 through the end of 2008 are used in this
171 study.

172

173 4.3. Data assimilation.

174

175 The GMAO assimilated ozone product is generated by ingesting OMI v8.5 total column ozone
176 and MLS v3.3 ozone profiles into the Goddard Earth Observing System version 5.7.2 (GEOS-
177 5.7.2) assimilation system with several modifications listed below. GEOS-5.7.2 is an updated
178 version of the global data assimilation system used to produce NASA's Modern Era
179 Retrospective Analysis (MERRA reanalysis) and described by Rienecker *et al.* [2011]. It
180 consists of an Atmospheric General Circulation Model (AGCM) and a statistical analysis module
181 that combines 6-hourly meteorological and chemical forecasts from the AGCM with

182 observational data from conventional measurements and satellite-borne sounders to produce an
183 analysis state. This AGCM is a version of the Fortuna general circulation model described in
184 *Molod et al.* [2012]. The statistical analysis is done using the Gridpoint Statistical Interpolation
185 (GSI) approach [*Wu et al.*, 2002; *Purser et al.*, 2003a, 2003b]. The assimilated product was
186 generated at a horizontal resolution of 2° latitude by 2.5° longitude and at 72 vertical layers
187 between the surface and 0.01 hPa. Depending on the height of the tropopause, about 25 to 35 of
188 those layers are in the troposphere.

189
190 Ozone profiles from the MLS retrievals are given on 38 levels between 261 hPa and 0.0215 hPa.
191 Prior to assimilation each profile is averaged in the vertical so that the mid-level average values
192 of the mixing ratios are assimilated. The averaging eliminates some of the negative ozone values
193 reported by MLS while preserving the integrated columns. In order to account for variable
194 sensitivity of total ozone measurements by the OMI instrument we use the efficiency factor
195 information (averaging kernels) provided with the data to weight the impact of these
196 observations in the vertical. The GSI convolves the forecast ozone profile at each OMI
197 observation location and the climatological *a priori* with their respective efficiency factors and
198 subtracts their sum from the observed value of the total ozone column. By doing this, the
199 dependence on OMI's *a priori* is largely removed in the assimilation. Although the row anomaly
200 has time dependence that affects a growing number of rows over the Aura record, the
201 assimilation uses the same OMI level-2 rows #2-24 over the entire record for consistency. The
202 GEOS-5 AGCM transports the assimilated ozone using the assimilated meteorology but
203 complete ozone chemistry is not accounted for. There is no model chemistry in the troposphere
204 and only a dry deposition mechanism at the surface is applied. This approach works well

205 because the ozone time scale is long compared to the 6 hours between analysis times when the
206 background field is corrected by observations. In the stratosphere the model applies time
207 dependent (monthly) zonally symmetric ozone production and loss rates derived from a two-
208 dimensional model as in *Stajner et al.* [2008]. This approach also works well for the same
209 reason of comparatively long ozone lifetimes in the lower stratosphere which contributes the
210 bulk of the total ozone column.

211

212 The main differences between the operational configuration of GEOS-5.7.2 and the system used
213 in this study are: (1) The use of MLS ozone data instead of Solar Backscatter Ultraviolet
214 observations, (2) the use of efficiency factors for OMI, (3) state dependent background error
215 covariances similar to those used in *Stajner et al.* [2008], and (4) the absence of an ozone
216 chemistry parameterization below the tropopause. Tests showed that the previous tropospheric
217 parameterization did not significantly impact the accuracy of the ozone in the troposphere
218 compared to ozonesonde measurements. A complete description of this system is given by
219 *Wargan et al.* [2013]. Ozonesonde validation of the assimilated ozone profiles is shown by
220 *Wargan et al.* [2013] and primarily focuses on the variability and structure of ozone in the upper
221 troposphere and lower stratosphere. Information that data assimilation has of tropospheric ozone
222 comes from OMI total column ozone which has reduced sensitivity in the low troposphere as
223 mentioned in section 2.

224

225 **5. Ozonesonde validation of the TCO products.**

226

227 Ozonesonde measurements are used to evaluate the TCO gridded products with the sonde station
228 locations shown in Figure 1. Ozonesonde profiles were integrated from ground to the tropopause
229 to derive daily TCO measurements that were then plotted against daily TCO from the three
230 global data products and the GMI CTM simulation. For the remainder of our study these are
231 abbreviated in figures and text as TRAJ, PROF, ASSIM, and GMI (corresponding to trajectory
232 mapping, nadir profile retrieval, GMAO data assimilation, and the GMI CTM, respectively).

233 Figure 2 shows TCO for the three data products and CTM plotted versus ozonesonde TCO where
234 all days of the years (years indicated in figure caption) and all latitudes for the sondes are
235 included. In Figure 2 the TRAJ, ASSIM, and GMI TCO measurements all use the same
236 tropopause pressures which come from the TRAJ data product. These tropopause pressures
237 include quality flagging which filters out highly dynamical conditions such as tropopause folds
238 which can produce large uncertainties in the derived column amounts. For the TRAJ TCO
239 product an additional filter is applied for clouds (i.e, only OMI scenes with reflectivity less than
240 0.3 are used) to nearly eliminate (down to ~1-2 DU) artificial ghost column ozone in TCO. For
241 the PROF TCO product the NCEP tropopause pressures were not filtered for either clouds or
242 highly dynamical conditions. For these reasons the values for N in Figure 2 for the three data
243 products are different and why N is similar between GMI and ASSIM.

244
245 In Figure 2 the variability for both product and sonde comes largely from seasonal cycles as well
246 as variations with latitude/region for the many station locations included for each scatter plot.
247 Statistical quantities listed in each of the four scatterplots include the mean offset (product or
248 model minus ozonesonde) and the difference RMS. Time averages were removed from all data

249 products/GMI and ozonesondes prior to calculating difference RMS numbers. Figure 2 is useful
250 in making baseline comparisons, but nothing can be said regarding latitudinal dependences.

251
252 Figure 3 shows the ozonesonde TCO comparisons of Figure 2 for separate latitude bands of 20°
253 to 40° intervals as described in the Figure 3 caption. The top, middle, and bottom panels in
254 Figure 3 plot differences from sonde values, difference RMS, and correlation between sonde
255 values with each product as well as the simulation. The total number of ozonesonde profiles
256 included in these calculations (“N”) is listed in the bottom panel of Figure 3.

257
258 The differences in Figure 3 (top) show that the ASSIM TCO and TRAJ TCO have the largest
259 offsets relative to ozonesondes. Despite near-zero offset for GMI in Figure 2, latitude
260 dependence of the offset for GMI in Figure 3 shows ~ 5 DU shift from the tropics to high
261 latitudes in both hemispheres. The difference RMS values in Figure 3 (middle) show
262 consistency between the three data products and model in the tropics and subtropics but in mid-
263 high latitudes, particularly in the SH the RMS numbers show greater spread between them. The
264 TRAJ TCO product has largest difference RMS numbers. Figure 3 (bottom) shows that all three
265 products and model have correlations $\sim +0.8$ in the tropics. Outside the tropics the smallest
266 correlations correspond to the TRAJ product, particularly in the SH. Largest correlation in
267 Figure 3 for any product is about $+0.85$.

268
269 The ozonesonde TCO comparisons are extended by examining individual seasons of the year
270 rather than entire year as in Figure 2. Figures 4-7 show scatter plots similar to Figure 2 but for
271 the four seasons December-January-February (DJF), March-April-May (MAM), June-July-

272 August (JJA), and September-October-November (SON) for each of the data products and GMI
273 CTM. There are several obvious characteristics in Figures 4-7 for the three data products and the
274 CTM model. The assimilated TCO in Figure 4 in each season is biased low by several DU
275 compared to the ozonesondes but the difference RMS numbers each season are small at only
276 about 5-7 DU. For PROF TCO in Figure 5 offsets are only a few DU but there are many
277 outliers, especially for the DJF. (These outliers drive the calculated difference RMS to nearly 10
278 DU.) The TRAJ TCO product in Figure 6 has the largest difference RMS and largest offsets
279 relative to sondes, however even the largest difference RMS in MAM is still about 9 DU or less
280 and the RMS numbers are only about 6 DU for JJA and SON seasons. For the GMI CTM in
281 Figure 7 the offsets are smaller in each season compared to the data products, yet the difference
282 RMS numbers are slightly larger each season compared to assimilated TCO.

283
284 In summary, we find that the ASSIM data product compares best overall with the ozonesondes.
285 Outside the tropics the trajectory mapping product has the largest bias and difference RMS
286 values. Statistics for the direct profile retrieval method are favorable in terms of a small average
287 bias relative to sondes, yet there is larger scatter and higher difference RMS with sondes than for
288 data assimilation. The GMI model has smallest offsets with the ozonesondes but has slightly
289 larger difference RMS values in each season when compared with the ASSIM product.

290
291 **6. Spatial variability of the ozone products.**

292
293 We next examine spatial characteristics of TCO and SCO for the three data products and GMI
294 CTM as functions of season to identify consistencies and differences between them. Seasonal

295 mean maps of TCO and SCO for the products and CTM are plotted in Figures 8-11 where TCO
296 and SCO in each figure are shown as part (a) and part (b), respectively. These seasonal averages
297 were obtained from eight-year time series (January 2005 – December 2012) with the exception
298 that the PROF measurements extend about four years from October 2004 through December
299 2008.

300
301 In the tropics, TCO for the data products and the GMI CTM in Figure 8 for DJF show a
302 characteristic zonal wave-one variability with largest ozone in the Atlantic and smallest ozone
303 over Indonesia. This wave-one zonal pattern occurs in all seasons with each product and the
304 CTM as evident from Figures 9-11. For ASSIM TCO the Pacific values are larger and zonal
305 amplitude of the wave-one pattern is smaller when compared to the other measurements and
306 CTM. The year-round nature of the wave pattern in tropical TCO was first shown by *Fishman et*
307 *al.* [1990] from combined TOMS and SAGE satellite measurements. Persistence of the wave-
308 one is due to the year-round east-west tropical Walker circulation in the troposphere. TCO in the
309 tropics maximizes in the Atlantic region during the SON season that corresponds to peak
310 biomass burning in tropical South America and Africa. Despite intense biomass burning,
311 *Sauvage et al.* [2007] suggests that the enhanced TCO in the Atlantic during SON is caused more
312 by lightning rather than biomass burning.

313
314 All three data products and GMI CTM have smallest global mean TCO during DJF (Figure 8a).
315 In MAM (Figure 9) TCO for all four have similar NH springtime buildup and horizontal
316 structure. By JJA (Figure 10) all products and CTM have largest TCO in the NH extra-tropics
317 with a corresponding buildup of TCO in the tropical/subtropical south Atlantic. The large TCO

318 in the NH extra-tropics during JJA is caused mostly by combination of stratosphere-troposphere
319 exchange, anthropogenic pollution, and lightning [e.g., *Leleiveld and Dentener, 2000*].

320
321 There are other basic characteristics of TCO and SCO in Figures 8-11. Spatial variability and
322 seasonal dependence of TCO over the course of the year are almost identical in general sense
323 between the three data products and GMI CTM. During DJF TCO in the SH polar region is as
324 small as in the tropical western Pacific. SCO in Figures 8-11 for all three data products and
325 CTM has small spatial variability throughout the tropics but large spatial variability and highest
326 column amounts in the mid-high latitudes in both hemispheres during winter-spring. SCO
327 during SON with all three products and CTM depict buildup of stratospheric ozone south of
328 Australia lying northward along the edge of the SH stratospheric polar vortex.

329
330 Although TCO and SCO in Figures 8-11 have consistent geophysical features during all seasons
331 there are also some inconsistencies. An example of this that we now examine more closely is the
332 zonal variability of TCO and SCO in the tropics. It was noted for Figures 8-11 that TCO for all
333 products in the tropics has a characteristic zonal wave-one pattern while SCO in the tropics
334 exhibits small zonal variability. In Figure 12 we show TCO for the four products along the
335 equator (Figure 12a) and corresponding SCO along the equator (Figure 12b) as time versus
336 longitude. TCO in Figure 12a for all data products and CTM has a similar wave-one pattern that
337 maximizes around September-October corresponding to the months of peak biomass burning
338 over Africa and South America. The wave-one pattern of TCO for ASSIM is larger year-round
339 in the Pacific by several DU when compared with the other data products and CTM.

340

341 There are some inconsistencies for SCO in Figure 12b between the three data products and GMI
342 CTM. TRAJ SCO in Figure 12b during any month has very small zonal variability of only a few
343 DU. This small zonal variability of SCO has been shown in previous studies using
344 measurements from MLS, SAGE, and HALOE satellite instruments, as well as ozonesondes
345 [e.g., *Fishman et al.*, 1990; *Ziemke et al.*, 1998; *Thompson, et al.*, 2003]. SCO in Figure 12b for
346 September (i.e., when largest SCO occurs) has zonal variability of ~10 DU for both the CTM
347 and ASSIM, whereas zonal variability of SCO for PROF is ~5 DU and only about 2-3 DU for
348 TRAJ. We can conclude from Figure 12 that the TRAJ product may be slightly better (by
349 several DU) at resolving zonal variability of tropical SCO compared to the other data products
350 and CTM.

351
352 We include lastly a statistical evaluation of the spatial variability of the three TCO data products
353 ASSIM, TRAJ, and PROF. This evaluation is listed in Tables 1-3 where a baseline reference
354 TCO field for each of the four seasons was calculated by averaging corresponding seasonal
355 means of the three data products and GMI CTM from Figures 8-11. Listed in Tables 1-3 for the
356 three data products are spatial correlations, offsets, and difference RMS numbers, respectively.
357 Positive correlations > 0.9 in Table 1 suggest highly consistent spatial variability but there are
358 also small correlations for the TRAJ and PROF products in the latitude bands 30°N-60°N and
359 30°S-60°S during winter. The mean offsets listed in Table 2 are for the most part self-
360 explanatory with largest offsets for TRAJ followed secondly by ASSIM. The spatial difference
361 RMS calculations for the data products in Table 3 are on average only about 1-2 DU. These low
362 RMS numbers show that the three data products have consistent zonal and meridional variations
363 of TCO during all seasons and in all latitude bands.

364

365 **7. Applications using the ozone products.**

366 The primary ozone product which we focus on for applications is ASSIM as this product
367 compares well with ozonesondes, has daily global coverage of long record, and provides ozone
368 profile information [e.g., *Wargan et al.*, 2013]. By comparison the TRAJ daily product does not
369 provide ozone profile information, and the PROF daily ozone profile product extends only
370 through year 2008 with coarse vertical resolution when compared with ASSIM. We discuss
371 some applications in this section using these ozone products involving case studies and inter-
372 annual variability.

373

374 7.1. Western Russia wildfires of year 2010 and pollution events

375

376 Record heat occurred over a broad region of western Russia in the summer of 2010 along with
377 related intense uncontrolled wildfires. A prolonged anti-cyclonic circulation over western Russia
378 caused sustained hot and dry conditions beginning in May 2010 and extending into early August
379 2010. This unusual meteorology created conditions favorable for wildfires. The breadth and
380 intensity of the wildfires were the largest since Aura instruments began observations in the
381 second half of 2004 [*Witte et al.*, 2011].

382

383 Figure 13 (top) plots monthly mean TCO for ASSIM, TRAJ, and GMI CTM for the burning
384 region in western Russia over the eight-year record. Peak levels of ozone are observed in July
385 2010 for the two data products and the CTM. In the bottom panel of Figure 13 daily ozone
386 profiles from ASSIM averaged over this region are plotted as log-pressure altitude versus day for

387 year 2010. The ozone profiles in Figure 13 are given as vertical column densities (in units DU-
388 km^{-1}) to indicate relative contribution to TCO as function of altitude. The ASSIM profile ozone
389 suggests that the anomalous increase in TCO in July 2010 extended throughout the troposphere
390 with most contribution coming from below ~ 6 km. This vertical distribution of tropospheric
391 ozone in July coincided with the anti-cyclonic blocking high observed by *Witte et al.* [2011] that
392 extended from the near surface through the free-troposphere.

393

394 Simulated increases in tropospheric ozone during the 2010 wildfire event suggest that anomalous
395 meteorology is the main driver of these ozone enhancements. As described in section 3 the
396 annual emissions for the GMI model for years 2009-2012 are a repeat of the 2008 emissions and
397 therefore the July 2010 enhanced TCO for the model in Figure 13 cannot be attributed directly to
398 a change in emissions. *Witte et al.* [2011] showed from satellite Outgoing Long-wave Radiation
399 (OLR) anomalously high tropospheric warming during summer 2010 over western Russia
400 compared to previous years 2003-2009. This suggests that meteorological change in summer
401 2010 is related directly to these increases in tropospheric ozone. The anomalous warming in
402 summer 2010 was associated with a persistent subsidence in the region and associated anti-
403 cyclonic circulation.

404

405 *Kar et al.* [2010] showed that OMI/MLS tropospheric ozone has signatures of pollution in urban
406 areas. However, while some urban regions showed local enhancement of tropospheric ozone,
407 other urban regions did not. One important issue with detecting urban pollution ozone from OMI
408 is that ozone sensitivity in the troposphere (which varies greatly with surface reflectivity
409 conditions) decreases on average from about 100% in the mid-upper troposphere down to about

410 40%-70% at 3 km altitude, and to only a few % (if not zero %) at the surface. Unless pollution
411 related ozone in the boundary layer is dynamically lifted upward it will not be readily detected
412 by OMI. It is well known that photochemical production of ozone in the troposphere requires
413 sufficient concentrations of NO_x and volatile organic compounds, sufficient UV radiation and
414 favorable meteorological conditions. Even drastic changes in pollution and ozone precursors
415 may not significantly change tropospheric ozone. *Witte et al.* [2009] showed from OMI
416 measurements that large reductions in tropospheric NO₂ and SO₂ occurred during the 2008
417 Olympics event compared to previous Aura years 2004-2007. These sharp reductions were
418 indicative of the rigorous pollution control measures implemented over eastern China prior to
419 and during the Olympics. Despite the large reductions in certain target pollutants we have found
420 no significant reductions in TCO over eastern China for either the TRAJ and ASSIM data
421 products or CTM (figures not shown).

422

423 We conclude that the daily ozone products illustrate that they can contribute to case studies
424 involving events such as the Russian fires and the 2008 Olympics. However, much of
425 tropospheric ozone variability occurs over longer timescales including annual cycles and inter-
426 annual periods. In the following we use the important property of long decadal records with the
427 OMI/MLS products to show applications involving inter-annual variability.

428

429 7.2. The tropical El Niño Southern Oscillation.

430

431 The tropical El Niño Southern Oscillation (ENSO) is the dominant source of inter-annual
432 changes of the tropical lower atmosphere and ocean. A description and historical account of

433 ENSO is given by *Trenberth* [1997; and references therein]. “ENSO” refers to either El Niño
434 (anomalously warm ocean temperatures in the tropical eastern Pacific) or La Niña (anomalously
435 cool ocean temperatures in the tropical eastern Pacific). Consecutive El Niño or La Niña events
436 have a varying periodicity of about 2-7 years and maximize during months around NH late
437 autumn to late winter.

438
439 A multi-decadal monthly tropospheric ozone ENSO index (OEI) was derived by *Ziemke et al.*
440 [2010] to monitor intensity of ENSO events in tropospheric ozone and to use as a diagnostic test
441 for models of atmospheric chemistry and transport. To calculate the OEI, TCO for each month is
442 first averaged over the eastern Pacific (15°S-15°N, 110°W-180°) and western Pacific (15°S-15°N,
443 70°E-140°E). (These two regions were chosen to maximize correlation between TCO and the
444 Niño 3.4 temperature anomaly ENSO index.) A monthly time series is then generated by taking
445 the difference of western minus eastern Pacific tropospheric ozone columns. This time series is
446 then deseasonalized, followed by a 3-month running average (to be consistent with calculation of
447 the monthly Niño 3.4 ENSO index).

448
449 Figure 14a plots the TCO OEI derived separately from ASSIM (dotted purple curve), PROF
450 (dashed blue curve), TRAJ (dotted-dashed green curve), and GMI (solid red curve). Also
451 included in Figure 14 is the Niño 3.4 index (solid black curve) and correlation “r” between Niño
452 3.4 and the four OEI’s. All four OEI’s extend from January 2005 through December 2012
453 except for PROF OEI which ends December 2008.

454

455 Each of the four OEI time series in Figure 14a are nearly identical and within about 1 DU from
456 each other each month. However, all four OEI's differ from Niño 3.4 at certain times of the
457 record. It can be shown from daily values that these discrepancies between the OEI's and Niño
458 3.4 coincide with intra-seasonal/Madden-Julian Oscillation (MJO) variability [*Madden and*
459 *Julian*, 1971, 1994, and references therein] in tropospheric ozone during NH winter-spring
460 months. Large discrepancy occurs around January 2008 (i.e., during La Niña) and shows all four
461 OEI's with relative maxima while Niño 3.4 has a relative minimum. Understanding the tropical
462 intra-seasonal variability/MJO and its coupling effect with ENSO and monthly OEI is beyond
463 the scope of our current study.

464

465 We show that the profile ozone from ASSIM may provide some further insight regarding the
466 vertical distribution of the OEI in tropospheric ozone. In Figure 14b ASSIM upper tropospheric
467 column ozone (dotted blue curve) is plotted with lower tropospheric column ozone (dashed red
468 curve) and Niño 3.4 (solid black curve). Upper and lower tropospheric column ozone in Figure
469 14b are defined as the ozone column between 500 hPa to tropopause and 500 hPa to ground,
470 respectively. The ASSIM ozone in Figure 14b indicates that most contribution to the OEI
471 originates in the upper troposphere above 500 hPa. The month-by-month changes in upper and
472 lower tropospheric ozone generally track each other over the long record, but two exceptions
473 occur. One exception is centered around January 2010 (El Niño) and another around January
474 2011 (La Niña). The ASSIM tropospheric profile ozone for these two cases suggests that upper
475 and lower tropospheric ozone in the tropical Pacific are not always coherent. Conclusions
476 regarding ASSIM tropospheric ozone profile information are not certain due to lack of a
477 tropospheric chemistry scheme and reduced OMI efficiency in the lower troposphere.

478

479 7.3. A global analysis of inter-annual variability of ozone.

480

481 General characteristics of inter-annual variability in global tropospheric and stratospheric ozone
482 are examined using the eight years of column ozone and profile ozone products. Figure 15
483 shows monthly zonal mean SCO (top panel) and TCO (bottom panel) from data assimilation.
484 Both SCO and TCO in Figure 15 have recurring seasonal patterns each year but with some years
485 indicating inter-annual change. For SCO there is a 2-3 year QBO cycle in the tropics and extra-
486 tropics and also anomalous enhanced SCO in the tropics and subtropics around the months
487 October 2010 – January 2011. Equatorial TCO for the final 2-3 years is slightly larger compared
488 to the previous years.

489

490 The inter-annual features in SCO and TCO are better identified by removing seasonal cycles in
491 the data. The SCO and TCO from ASSIM in Figure 15 were deseasonalized and re-plotted in
492 Figure 16a to better identify inter-annual differences and near-decadal changes. For comparison
493 with ASSIM, deseasonalized SCO and TCO from TRAJ measurements are shown in Figure 16b.
494 The SCO and TCO products from ASSIM and TRAJ in Figure 16 are equivalent everywhere to
495 within a few Dobson Units. Figure 16 shows that both SCO products have a clear QBO in the
496 tropics and throughout the SH, but in the NH the QBO signal for SCO is mixed with other inter-
497 annual changes occurring in mid-high latitudes (discussed later).

498 It can be shown for all data products including the GMI CTM that even though inter-annual
499 changes of TCO on a regional basis may constitute many DU, inter-annual changes for zonal
500 mean TCO are exceedingly small. Figure 16 shows that inter-annual variability of zonal mean

501 TCO is only about 1-2 DU on average for ASSIM and TRAJ. This shows that most all inter-
502 annual change present in zonal mean total column ozone is due to inter-annual change in SCO.
503 Both zonal mean TCO products in Figure 16 also show small increases in the latter years of the
504 record. This is currently being investigated using the GMI model (figures not shown) which also
505 shows small net increase in TCO in the latter years during predominantly La Nina conditions
506 (particularly the strong La Nina event centered around January 2011). *Doherty et al.* [2006]
507 indicated from a coupled chemistry climate model that the shift from El Niño to La Niña
508 conditions in the troposphere may produce several percent increase in the total ozone burden.
509 This is not inconsistent with the small net increases we find in tropical tropospheric ozone in
510 Figure 16.

511
512 In Figures 17-19 we show inter-annual variability of zonal mean ozone profile densities (in DU-
513 km^{-1}) for selected latitude bands in correspondence to the 8-year record of column ozone in
514 Figure 16. In Figure 17 deseasonalized ozone profiles from ASSIM (top) are plotted with ozone
515 profiles from MLS (bottom) for general one-to-one comparison. Largest contribution to the
516 equatorial QBO shown earlier in Figure 16 lies within the vertical band of about 20-25 km in
517 log-pressure altitude in Figure 17. Figure 18 compares ASSIM ozone profile densities at 40°N
518 and 40°S. Ozone profiles in the SH at 40°S in Figure 18 have a clear 2-3 year QBO signal
519 (which is mostly out-of-phase with the equatorial QBO signal), but not so for the NH because of
520 other additional inter-annual changes. Most stratospheric ozone inter-annual variability in both
521 the NH and SH mid-latitudes lies around 20 km.

522 ASSIM deseasonalized ozone profiles are plotted again in Figure 19 as in the previous figure but
523 instead for high polar latitudes 80°N and 80°S. Largest inter-annual variability at 80°N in Figure

524 19 occurs during winter when OMI has no ozone measurements because of polar night. Several
525 enhanced inter-annual changes in ozone in Figure 19 associated with sudden stratospheric
526 warming events occur in the northern polar region. These NH warming events are identified in
527 Figure 19 as large inter-annual changes during winter-spring months. Two intense stratospheric
528 warming events in the NH during winter months are identified in 2006 and 2009. At least three
529 stratospheric warmings in Figure 19 coincide with Arctic split events [e.g., *Ripesi et al.*, 2012] in
530 spring 2005, winter 2009, and winter 2010. For each split event the ASSIM ozone has a relative
531 minimum in the vertical centered around 15 km. These relative minima in the lower stratosphere
532 are not present for other warming events such as 2006 and 2011. As a note, winter-spring 2011
533 in Figure 19 indicates reductions of ozone rather than increases in the lower stratosphere. The
534 anomalous reduction of stratospheric ozone in March 2011 was largely explained in recent
535 studies by *Manney et al.* [2011], *Isaksen et al.* [2012], and *Strahan et al.* [2013] as an unusually
536 strong polar vortex that year which suppressed and delayed the transport of stratospheric ozone
537 from lower latitudes. Inter-annual variability in the SH polar region in Figure 19 (bottom) is
538 small when compared to the NH polar region. For the SH two anomalous events (exceeding +5
539 DU-km⁻¹) occurred in the range 20-25 km during October-November in 2005 and 2012. These
540 two events signify anomalously high stratospheric ozone levels in the immediate lower
541 stratosphere polar region during Antarctic ozone depletion conditions.

542

543 **8. Summary.**

544

545 Three different strategies to obtain tropospheric and stratospheric ozone from Aura OMI/MLS
546 measurements beginning late 2004 have been evaluated for their overall data quality and

547 usefulness for science applications. These three strategies are trajectory mapping (denoted
548 TRAJ), direct profile retrieval (denoted PROF), and data assimilation (denoted ASSIM). The
549 evaluation of the three products includes validation using ozonesondes and comparisons with the
550 Global Modeling Initiative (GMI) chemical transport model (CTM).

551
552 The three OMI/MLS ozone data products were compared with ozonesonde measurements from
553 WOUDC, SHADOZ, and NDACC. The TRAJ tropospheric column ozone (TCO) product was
554 shown to have the largest bias (i.e., a low bias exceeding 5 DU on average) relative to the
555 sondes. This low bias is mostly due to MLS ozone being high biased in the low stratosphere
556 [e.g. *Livesey et al.*, 2011] and a calibration offset between OMI v8.5 and MLS v3.3
557 measurements. The ASSIM TCO also has a low bias but it is reduced by better accounting for
558 measurement uncertainties/noise that also reduces RMS differences with sondes. RMS
559 differences are smallest and correlations are closest to one for the ASSIM ozone.

560
561 The daily ozone products are demonstrated to be useful for evaluating regional case studies such
562 as the 2010 Russian wildfires and the 2008 Beijing Olympics. In summer 2010 intense wildfires
563 persisted in western Russia caused by anomalously dry conditions. Tropospheric ozone was
564 largest in all of the products and the GMI CTM during July 2010 compared to any other month
565 of the 2005-2012 record. The anomalous increase in tropospheric ozone in western Russia was
566 about 5 DU compared to an average background of around 35 DU. Tropospheric ozone profiles
567 from data assimilation indicate that the anomalous increases in tropospheric ozone in July 2010
568 extended deep throughout the troposphere with most contribution coming from the lower
569 troposphere below 500 hPa. The ozone increases coincided with anomalous meteorological

570 conditions that year involving an unusual stationary high pressure blocking event and warm
571 temperatures.

572

573 The photochemical production of tropospheric ozone is sensitive to the concentrations of NO_x
574 and volatile organic compounds (VOC's), UV radiation, and meteorological conditions. Drastic
575 changes in ozone precursors may not necessarily coincide with measureable changes in
576 tropospheric ozone. A case study example of this effect was the 2008 Beijing Olympics whereby
577 there were large reductions in regional pollution including ozone precursors, yet OMI/MLS data
578 products and the CTM all showed no reduction in tropospheric ozone.

579

580 With the Aura OMI and MLS measurements beginning late 2004, the ozone product records are
581 now long enough to study and characterize inter-annual to near-decadal variability of
582 stratospheric and tropospheric ozone. The OMI/MLS ozone products show that while the quasi-
583 biennial oscillation (QBO) is the dominant source of inter-annual variability of stratospheric
584 ozone in the tropics and SH, variability of stratospheric ozone in the NH includes an additional
585 mix of anomalous inter-annual increases and decreases. During the Aura record there were
586 several events of stratospheric sudden warmings in the NH including split events. These sudden
587 warmings occur in polar latitudes around winter months when there are no OMI ozone
588 measurements due to polar night. MLS stratospheric ozone profiles also do not fully cover the
589 polar region and do not "fill in" the ozone profiles missing between orbit paths as assimilation
590 does.

591

592 It is well known that the El Niño Southern Oscillation (ENSO) is the dominant source of inter-
593 annual change in tropospheric ozone in the tropical Pacific. The tropospheric ozone ENSO
594 index (OEI) of *Ziemke et al.* [2010] was calculated for the three data products and the CTM for
595 the 8-year Aura record. OEI derived for the three products and CTM are all remarkably
596 consistent to within about 1 DU from each other every month. Ozone profiles from data
597 assimilation suggest further that the OEI is driven mostly by ENSO forced ozone variations in
598 the upper troposphere above 500 hPa.

599

600 The three ozone data products and the CTM show that zonal mean tropospheric column ozone
601 has small inter-annual change of about 1-2 DU in any latitude range. The three data products
602 and CTM also show slight increase of 2-4 DU in tropospheric ozone toward the end of the Aura
603 record (i.e., years 2010-2012); the CTM suggests that this may be due in part to La Nina
604 conditions persisting in the tropics toward the end of the Aura record (this is ongoing work
605 beyond our current study).

606

607 When based upon ozonesonde validation and the broad set of science applications investigated,
608 the ASSIM ozone is overall the most useful of the three OMI/MLS data products. The
609 assimilated ozone provides a continuous global record of ozone which includes profile
610 information. Profile information for ozone is not provided by the TRAJ product and the PROF
611 profile product has a shorter record (through 2008) and comparatively coarse vertical resolution
612 for ozone profiles. Despite lack of profile information there are benefits of using the TRAJ daily
613 ozone product. The TRAJ product provides a long record of ozone and includes additional
614 geophysical parameters within the product files such as in situ cloud fractions and cloud

615 pressures, tropopause pressures (various definitions), and tropospheric and stratospheric column
616 amounts (using various tropopause pressure definitions), etc.

617 The GMAO assimilated ozone in our study is currently a preliminary product that will at later
618 time be made available to the public following further validation by *Wargan et al.* [2013].
619 Information about using the TRAJ product can be obtained from the NASA Goddard ozone air
620 quality website <http://ozoneaq.gsfc.nasa.gov/>.

621 **References**

622

623 Doherty, R. M., D. S. Stevenson, C. E. Johnson, W. J. Collins, and M. G. Sanderson,
624 Tropospheric ozone and El Niño–Southern Oscillation: Influence of atmospheric dynamics,
625 biomass burning emissions, and future climate change, *J. Geophys. Res.*, *111*, D19304,
626 doi:10.1029/2005JD006849, 2006.

627 Duncan, B.N., S.E. Strahan, Y. Yoshida, S.D. Steenrod, and N. Livesey, Model Study of the
628 Cross-Tropopause Transport of Biomass Burning Pollution, *Atmos. Chem. Phys.*, *7*, 3713-3736,
629 2007.

630 Duncan, B. N., J. J. West, Y. Yoshida, et al., The influence of European pollution on ozone in
631 the Near East and northern Africa, *Atmos. Chem. Phys.*, *8*, 22-2283, 2008.

632

633 Fishman, J., and J. C. Larsen, Distribution of total ozone and stratospheric ozone in the tropics:
634 Implications for the distribution of tropospheric ozone, *J. Geophys. Res.*, *92*, 6627-6634,
635 doi:10.1029/JD092iD06p06627, 1987.

636

637 Fishman, J., C. E. Watson, J. C. Larsen, and J. A. Logan, Distribution of tropospheric ozone
638 determined from satellite data, *J. Geophys. Res.*, 95(D4), 3599-3617,
639 doi:10.1029/JD095iD04p03599, 1990.

640

641 Fishman, J., A. E. Wozniak, and J. K. Creilson, Global distribution of tropospheric ozone from
642 satellite measurements using the empirically corrected tropospheric ozone residual technique:
643 Identification of the regional aspects of air pollution, *Atmos. Chem. Phys.*, 3, 893-907,
644 doi:10.5194/acp-3-893-2003, 2003.

645

646 Foltz, G. R., and M. J. McPhaden, The 30-70 day oscillations in the tropical Atlantic, *Geophys.*
647 *Res. Lett.*, 31(15), L15205, 2004.

648

649 Foltz, G. R., and M. J. McPhaden, Mixed layer heat balance on intraseasonal time scales in the
650 northwestern tropical Atlantic Ocean, *J. Clim.*, 18(20), 4168-4187, 2005.

651

652 Hudson, R. D., and A. M. Thompson, Tropical tropospheric ozone from total ozone mapping
653 spectrometer by a modified residual method, *J. Geophys. Res.*, 103, D17, 22,129-22,145,
654 doi:10.1029/98JD00729, 1998.

655

656 Isaksen, I. S. A., C. Zerefos, W. C. Wang, D. Balis, K. Eleftheratos, B. Rognerud, F. Stordal, T.
657 K. Bernsten, J. H. LaCasce, O. A. Sovde, D. Olivie, Y. J. Orsolini, I. Zyrichidou, M. Prather, and

658 O. N. E. Tuinder, Attribution of the arctic ozone column deficit in March 2011, *Geophys. Res.*
659 *Lett.*, *39*, L24810, doi:10.1029/2012GL053876, 2012.

660

661 Kiladis, G. N., K. H. Straub, G. C. Reid, and K. S. Gage, Aspects of interannual and
662 intraseasonal variability of the tropopause and lower stratosphere, *Q. J. R. Meteorol. Soc.*, *127*,
663 *576*, 1961-1983, doi:10.1256/smsqj.57605, 2001.

664

665 Kar, J., J. Fishman, J. K. Creilson, A. Richter, J. R. Ziemke, and S. Chandra, Are there urban
666 signatures in the tropospheric ozone column products derived from satellite measurements?,
667 *Atmos. Chem. Phys.*, *10*, 5213-5222, doi:10.5194/acp-10-5213-2010, 2010.

668

669 Kim, J. H., M. J. Newchurch, and K. Han, Distribution of tropical tropospheric ozone
670 determined by the scan-angle method applied to TOMS measurements, *J. Atmos. Sci.*, *58*, *18*,
671 *2699-2708*, doi:10.1175/1520-0469(2001)058<2699:DOTTOD>2.0.CO;2, 2001.

672

673 Liu, X., P. K. Bhartia, K. Chance, R. J. D. Spurr, and T. P. Kurosu, Ozone profile retrievals from
674 the Ozone Monitoring Instrument, *Atmos. Chem. Phys.*, *10*, 2521-2537, 2010a.

675

676 Liu, X., P. K. Bhartia, K. Chance, L. Froidevaux, R. J. D. Spurr, and T. P. Kurosu, Validation of
677 Ozone Monitoring Instrument (OMI) ozone profiles and stratospheric ozone columns with
678 Microwave Limb Sounder (MLS) measurements, *Atmos. Chem. Phys.*, *10*, 2539-2549, 2010b.

679

680 Livesey, N. J., W. G. Read, L. Froidevaux, A. Lambert, G. L. Manney, H. C. Pumphrey, M. L.
681 Santee, M. J. Schwartz, S. Wang, R. E. Cofield, D. T. Cuddy, R. A. Fuller, R. F. Jarnot, J. H.
682 Jiang, B. W. Knosp, P. C. Stek, P. A. Wagner, and D. L. Wu, EOS MLS Version 3.3 Level 2
683 data quality and description document, Tech. rep., Jet Propulsion Laboratory, available from
684 <http://mls.jpl.nasa.gov/>, 2011.

685

686 Madden, R. A., and P. R. Julian, Description of the 40-50 day oscillation in the zonal wind in the
687 tropical Pacific, *J. Atmos., Sci.*, 28, 702-708, 1971.

688

689 Madden, R. A., and P. R. Julian, Observations of the 40-50 day tropical oscillation – a review,
690 *Mon. Wea., Rev.*, 122, 814-837, 1994.

691

692 Manney, G. L., Unprecedented Arctic ozone loss in 2011, *Nature*, 478, 469-475,
693 doi:10.1038/nature10556, 2011.

694

695 McPeters, R. D., G. J. Labow, and J. A. Logan, Ozone climatological profiles for satellite
696 retrieval algorithms, *J. Geophys. Res.*, 112, D5, D05308, doi:10.1029/2005JD006823, 2007.

697

698 Molod, A., L. Takacs, M. Suarez, J. Bacmeister, I.-S. Song, and A. Eichmann, The GEOS-5
699 Atmospheric General Circulation Model: Mean Climate and Development from MERRA to
700 Fortuna. NASA Technical Report Series on Global Modeling and Data Assimilation, NASA
701 TM-2012-104606, Vol. 28, 117 pp. http://gmao.gsfc.nasa.gov/pubs/tm/archive/tm_2012.php,
702 2012.

703
704 Newchurch, M. J., X. Liu, J. H. Kim, Lower-tropospheric ozone (LTO) derived from TOMS
705 near mountainous regions, *J. Geophys. Res.*, *106*, D17, 20,403-20,412,
706 doi:10.1029/2000JD000162, 2001.

707
708 Park, C.-K., and S. D. Schubert, Remotely forced intraseasonal oscillations over the tropical
709 Atlantic, *J. Atmos. Sci.*, *50*, 89-103, 1993.

710
711 Purser, R. J., W.-S. Wu, D. F. Parrish, and N. M. Roberts, Numerical aspects of the application
712 of recursive filters to variational statistical analysis. Part I: spatially homogeneous and isotropic
713 Gaussian covariances, *Mon. Wea. Rev.*, *131*, 1524-1535, 2003a.

714
715 Purser, R. J., W.-S. Wu, D. F. Parrish, and N. M. Roberts, Numerical aspects of the application
716 of recursive filters to variational statistical analysis. Part II: spatially inhomogeneous and
717 anisotropic general covariances, *Mon. Wea. Rev.*, *131*, pp. 1536-1548, 2003b.

718
719 Randel, W. J., and F. Wu, A stratospheric ozone profile data set for 1979-2005: Variability,
720 trends, and comparisons with column ozone data, *J. Geophys. Res.*, *112*, D06313,
721 doi:10.1029/2006JD007339, 2007.

722
723 Rienecker, M.M., M.J. Suarez, R. Gelaro, R. Todling, J. Bacmeister, E. Liu, M.G. Bosilovich,
724 S.D. Schubert, L. Takacs, G.-K. Kim, S.E. Bloom, J. Chen, D. Collins, A. Conaty, A. da Silva,
725 W. Gu, J. Joiner, R.D. Koster, R. Lucchesi, A. Molod, T. Owens, S. Pawson, P. Pegion, C.R.

726 Redder, R. Reichle, F.R. Robertson, A.G. Ruddick, M. Sienkiewicz, J. Woollen, MERRA -
727 NASA's Modern-Era Retrospective Analysis for Research and Applications, *J. Climate*, 24,
728 doi:10.1175/JCLI-D-11-00015.1, 2011.

729

730 Ripesi, P., F. Ciciulla, F. Maimone, and V. Pelino, The February 2010 Arctic Oscillation Index
731 and its stratospheric connection, *Q. J. R. Meteorol. Soc.*, 138, 1961-1969, doi:10.1002/qj.1935,
732 2012.

733

734 Rui, H., and B. Wang, Development characteristics and dynamic structure of tropical
735 intraseasonal convection anomalies. *J. Atmos. Sci.*, 47, 357,379, 1990.

736

737 Sassi, F., M. Salby, H. C. Pumphrey, and W. G. Read, Influence of the Madden-Julian
738 Oscillation on upper tropospheric humidity, *J. Geophys. Res.*, 107, D23, 4681,
739 doi:10.1029/2001JD001331, 2002.

740

741 Sauvage, B., R. V. Martin, A. van Donkelaar, and J. R. Ziemke, Quantification of the factors
742 controlling tropical tropospheric ozone and the South Atlantic maximum, *J. Geophys. Res.*,
743 112(D11) D11309, doi:1029/2006JD008008, 2007.

744

745 Schoeberl, M. R., J. R. Ziemke, B. Bojkov, N. Livesey, B. Duncan, S. Strahan, L. Froidevaux, S.
746 Kulawik, P. K. Bhartia, S. Chandra, P. F. Levelt, J. C. Witte, A. M. Thompson, E. Cuevas, A.
747 Redondas, D. W. Tarasick, J. Davies, G. Bodeker, G. Hansen, B. J. Johnson, S. J. Oltmans, H.
748 Vomel, M. Allaart, H. Kelder, M. Newchurch, S. Godin-Beekmann, G. Ancellet, H. Claude, S.

749 B. Andersen, E. Kyro, M. Parrondos, M. Yela, G. Zablocki, D. Moore, H. Dier, P. von der
750 Gathen, P. Viatte, R. Stubi, B. Calpini, P. Skrivankova, V. Dorokhov, H. de Backer, F. J.
751 Schmidlin, G. Coetzee, M. Fujiwara, V. Thouret, F. Posny, G. Morris, J. Merrill, C. P. Leong, G.
752 Koenig-Langlo, and E. Joseph, A trajectory-based estimate of the tropospheric ozone column
753 using the residual method, *J. Geophys. Res.*, *112*, D24S49, doi:10.1029/2007JD008773, 2007.

754

755 Stajner, I., K. Wargan, S. Pawson, H. Hayashi, L-P. Chang, R.C. Hudman, L. Froidevaux, N.
756 Livesey, P.F. Levelt, A.M. Thompson, D.W. Tarasick, R. Stubi, S.B. Andersen, M. Yela, G.
757 Konig-Langlo, F.J. Schmidlin, and J. C. Witte, Assimilated ozone from EOS-Aura: evaluation of
758 the tropopause region and tropospheric columns, *J. Geophys. Res.* *113*, D16S32,
759 doi:10.1029/2007JD008863, 2008.

760 Strahan, S. E., B. N. Duncan, and P. Hoor, Observationally-derived diagnostics of transport in
761 the lowermost stratosphere and their application to the GMI chemistry transport model, *Atmos.*
762 *Chem. Phys.*, *7*, 2435-2445, 2007.

763

764 Strahan, S. E., A. R. Douglass, and P. A. Newman, the contributions of chemistry and transport
765 to low arctic ozone in March 2011 derived from Aura MLS observations, *J. Geophys. Res.*, *118*,
766 1563-1576, doi:10.1002/jgrd.50181, 2013.

767

768 Thompson, A. M., J. C. Witte, S. J. Oltmans, F. J. Schmidlin, J. A. Logan, M. Fujiwara, W. Volker, W. J.
769 H. Kirchhoff, F. Posny, G. J. R. Coetzee, B. Hoegger, S. Kawakami, T. Ogawa, J. P. F. Fortuin, and H.
770 M. Kelder, Southern Hemisphere Additional Ozonesondes (SHADOZ) 1998-2000 tropical ozone

771 climatology 2. Tropospheric variability and the zonal wave-one, *J. Geophys. Res.*, 108, D2, 8241,
772 doi:10.1029/2002JD002241, 2003.

773

774 van der Werf, G. R., J. T. Randerson, L. Giglio, G. J. Collatz, P. S. Kasibhatla, and A. F.
775 Arellano, Interannual variability in global biomass burning emissions from 1997 to 2004, *Atmos.*
776 *Chem. Phys.*, 6, 3423-3441, 2006.

777

778 Wargan, K., S. Pawson, M. Olsen, J. Witte, A. Douglass, J. Ziemke, S. Strahan, The Global
779 Structure of Ozone in the UTLS Region in an Assimilation of EOS-Aura Data, in preparation,
780 2013.

781

782 Witte, J. C., M. R. Schoeberl, A. R. Douglass, J. F. Gleason, N. A. Krotkov, J. C. Gille, K. E.
783 Pickering, and N. Livesey, Satellite observations of changes in air quality during the 2008
784 Beijing Olympics and Paralympics, *Geophys. Res. Lett.*, 36, L17803,
785 doi:10.1029/2009GL039236, 2009.

786

787 Witte, J. C., A. R. Douglass, A. da Silva, O. Torrs, R. Levy, and B. N. Duncan, NASA A-Train
788 and Terra observations of the 2010 Russian wildfires, *Atmos. Chem. Phys.*, 11, 9287-9301,
789 doi:10.5194/acp-11-9287-2011, 2011.

790

791 Wu, W.-S., R. J. Purser, and D. F. Parrish, Three-dimensional variational analysis with spatially
792 inhomogeneous covariances, *Mon. Wea. Rev.*, 130, 2905-2916, 2002.

793

794 Ziemke, J. R., S. Chandra, and P. K. Bhartia, Two new methods for deriving tropospheric
795 column ozone from TOMS measurements: The assimilated UARS MLS/HALOE and
796 convective-cloud differential techniques, *J. Geophys. Res.*, *103*, 22,115-22,127, 1998.

797
798 Ziemke, J. R., S. Chandra, B. N. Duncan, L. Froidevaux, P. K. Bhartia, P. F. Levelt, and J. W.
799 Waters, Tropospheric ozone determined from Aura OMI and MLS: Evaluation of measurements
800 and comparison with the Global Modeling Initiative's Chemical Transport Model, *J. Geophys.*
801 *Res.*, *111*, D19303, doi:10.1029/2006JD007089, 2006.

802
803 Ziemke, J. R., S. Chandra, B. N. Duncan, M. R. Schoeberl, M. R. Damon, O. Torres, and P. K.
804 Bhartia, Recent biomass burning events in the tropics and elevated concentrations of
805 tropospheric ozone, *Geophys. Res. Lett.*, *36*, L15819, doi:10.1029/2009GL039303, 2009.

806
807 Ziemke, J. R., S. Chandra, L. D. Oman, and P. K. Bhartia, A new ENSO index derived from
808 satellite measurements of column ozone, *Atmos. Chem. Phys.*, *10*, 3711-3721, 2010.

809

810

811

812

813

814

815

816 **Table 1.** Spatial correlation between product TCO and mean field TCO within four latitude
817 bands beginning with northern-most at the top. Calculations are done for three-month seasons of
818 December-February, March-May, June-August, and September-November (DJF, MAM, JJA,
819 SON, respectively). Each latitude band is comprised of 432 latitude-longitude grid points at
820 $5^{\circ} \times 5^{\circ}$ resolution.

821	Product	Latitudes	DJF	MAM	JJA	SON
822	ASSIM	30N-60N	0.92	0.93	0.91	0.95
823	TRAJ	30N-60N	0.77	0.94	0.97	0.93
824	PROF	30N-60N	0.81	0.95	0.96	0.96
825	ASSIM	0-30N	0.94	0.97	0.97	0.93
826	TRAJ	0-30N	0.96	0.99	0.98	0.97
827	PROF	0-30N	0.96	0.99	0.97	0.97
828	ASSIM	0-30S	0.94	0.93	0.97	0.97
829	TRAJ	0-30S	0.98	0.98	0.93	0.97
830	PROF	0-30S	0.97	0.94	0.93	0.95
831	ASSIM	30S-60S	0.99	0.98	0.93	0.99
832	TRAJ	30S-60S	0.99	0.92	0.65	0.93
833	PROF	30S-60S	0.99	0.98	0.92	0.98

834

835

836

837

838 **Table 2.** Similar to Table 1 but instead for product TCO minus mean field TCO difference in
839 Dobson Units.

840	Product	Latitudes	DJF	MAM	JJA	SON
841	ASSIM	30N-60N	-3.10	-2.74	-2.85	-5.15
842	TRAJ	30N-60N	-8.53	-7.32	-6.68	-8.33
843	PROF	30N-60N	1.73	3.19	1.63	1.72
844	ASSIM	0-30N	-2.48	-1.48	-0.37	-1.66
845	TRAJ	0-30N	-7.93	-7.04	-6.52	-6.66
846	PROF	0-30N	-1.96	-1.92	-1.63	-1.83
847	ASSIM	0-30S	-0.58	-0.88	-2.15	-1.92
848	TRAJ	0-30S	-6.88	-7.13	-8.22	-6.92
849	PROF	0-30S	-1.58	-2.15	-1.27	0.22
850	ASSIM	30S-60S	-0.17	-1.25	0.00	-0.81
851	TRAJ	30S-60S	-6.63	-7.15	-7.03	-6.77
852	PROF	30S-60S	-0.46	0.19	0.47	1.83

853

854

855

856

857

858

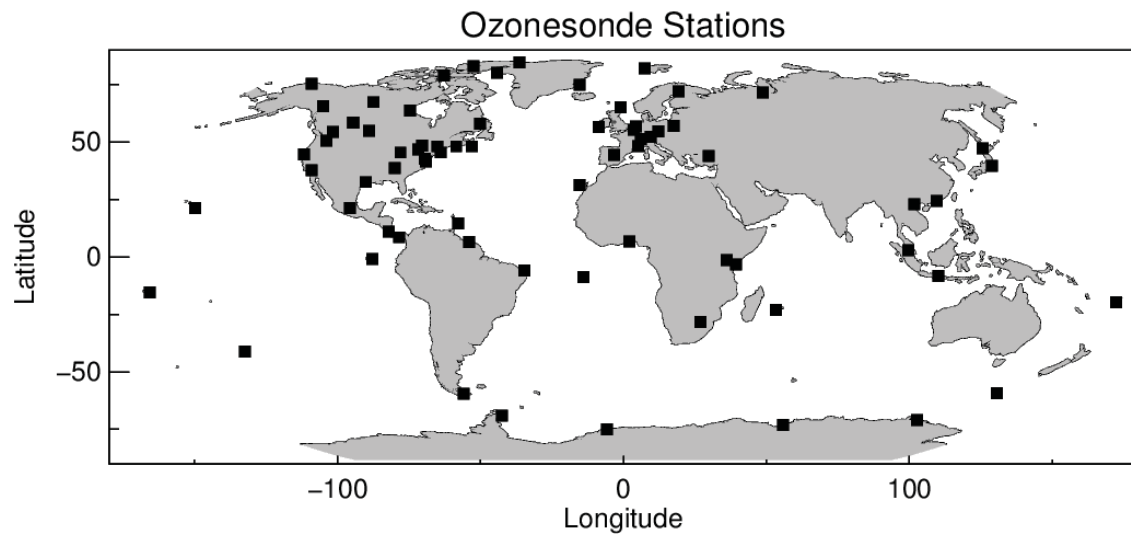
859

860

861 **Table 3.** Similar to Table 1 but instead for the difference RMS of Product TCO minus mean
 862 field TCO in Dobson Units. All TCO averages were removed prior to calculation of these
 863 difference RMS numbers.

864	Product	Latitudes	DJF	MAM	JJA	SON
865	ASSIM	30N-60N	1.23	1.52	2.00	1.26
866	TRAJ	30N-60N	2.22	1.52	1.13	1.35
867	PROF	30N-60N	3.04	1.46	1.38	1.08
868	ASSIM	0-30N	1.82	2.19	1.70	2.07
869	TRAJ	0-30N	1.32	1.10	1.16	1.24
870	PROF	0-30N	1.54	1.77	1.56	1.33
871	ASSIM	0-30S	1.73	1.53	1.18	1.74
872	TRAJ	0-30S	0.97	0.95	1.84	1.74
873	PROF	0-30S	1.34	1.58	2.48	3.01
874	ASSIM	30S-60S	0.77	0.62	0.93	0.79
875	TRAJ	30S-60S	0.86	1.18	2.11	1.75
876	PROF	30S-60S	0.98	0.64	1.72	2.05

877
 878
 879
 880
 881
 882
 883



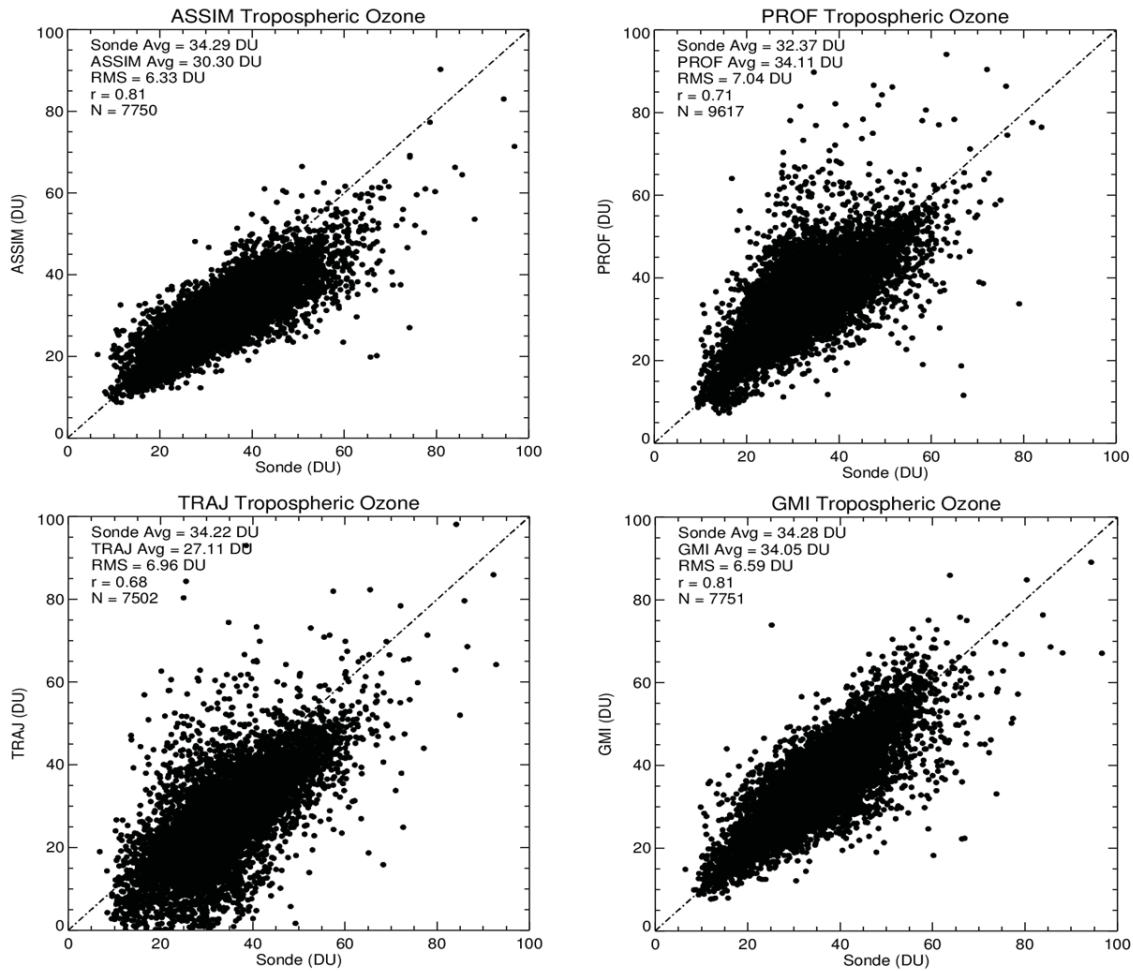
884

885 **Figure 1.** Geo-location sites for ozonesondes used in our study for validation of the ozone
886 products. The ozonesonde data are daily ozone profile measurements from SHADOZ, WOUDC,
887 and NDACC.

888

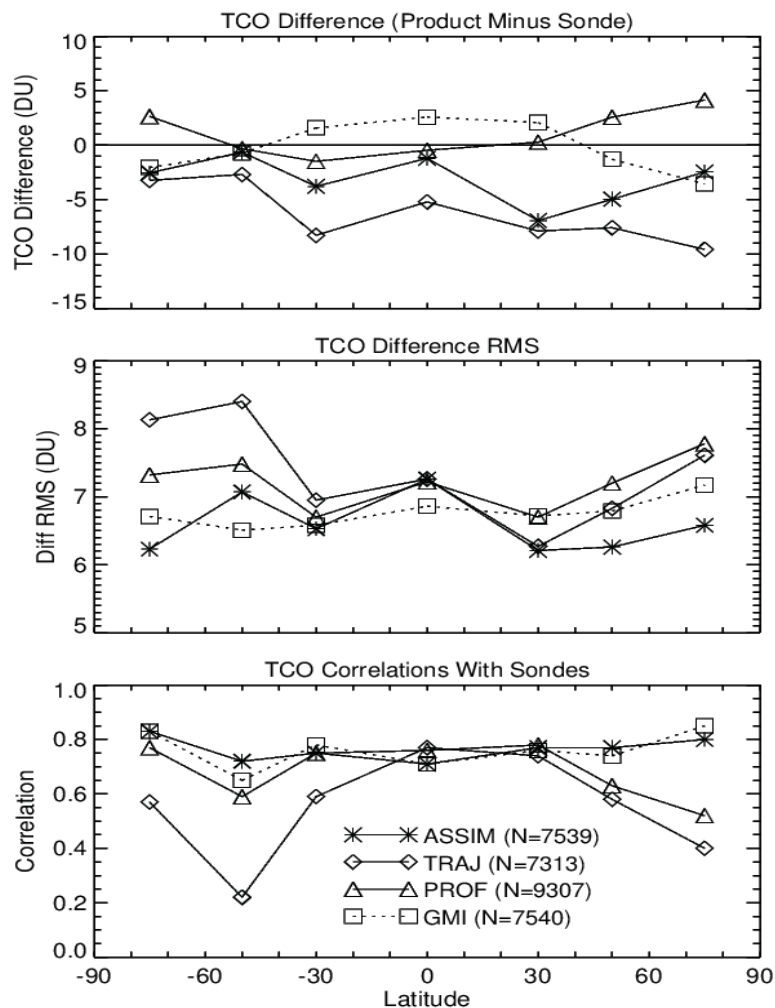
889

Ozonesonde TOR Scatter Plots for Global Gridded Products: All Ground Stations Between 90°S and 90°N



890

891 **Figure 2.** Daily TCO for the four products (data assimilation, direct profile retrieval, trajectory
 892 mapping, and GMI model) plotted versus coincident ozonesonde TCO. Included for each
 893 product in the scatter plots are their averages, difference RMS value, correlation, and total
 894 number of data pairs. The 1-1 line is also shown. The years included for ozonesonde
 895 comparisons for PROF are 2004-2008 and 2005-2010 for GMI, TRAJ, and ASSIM.



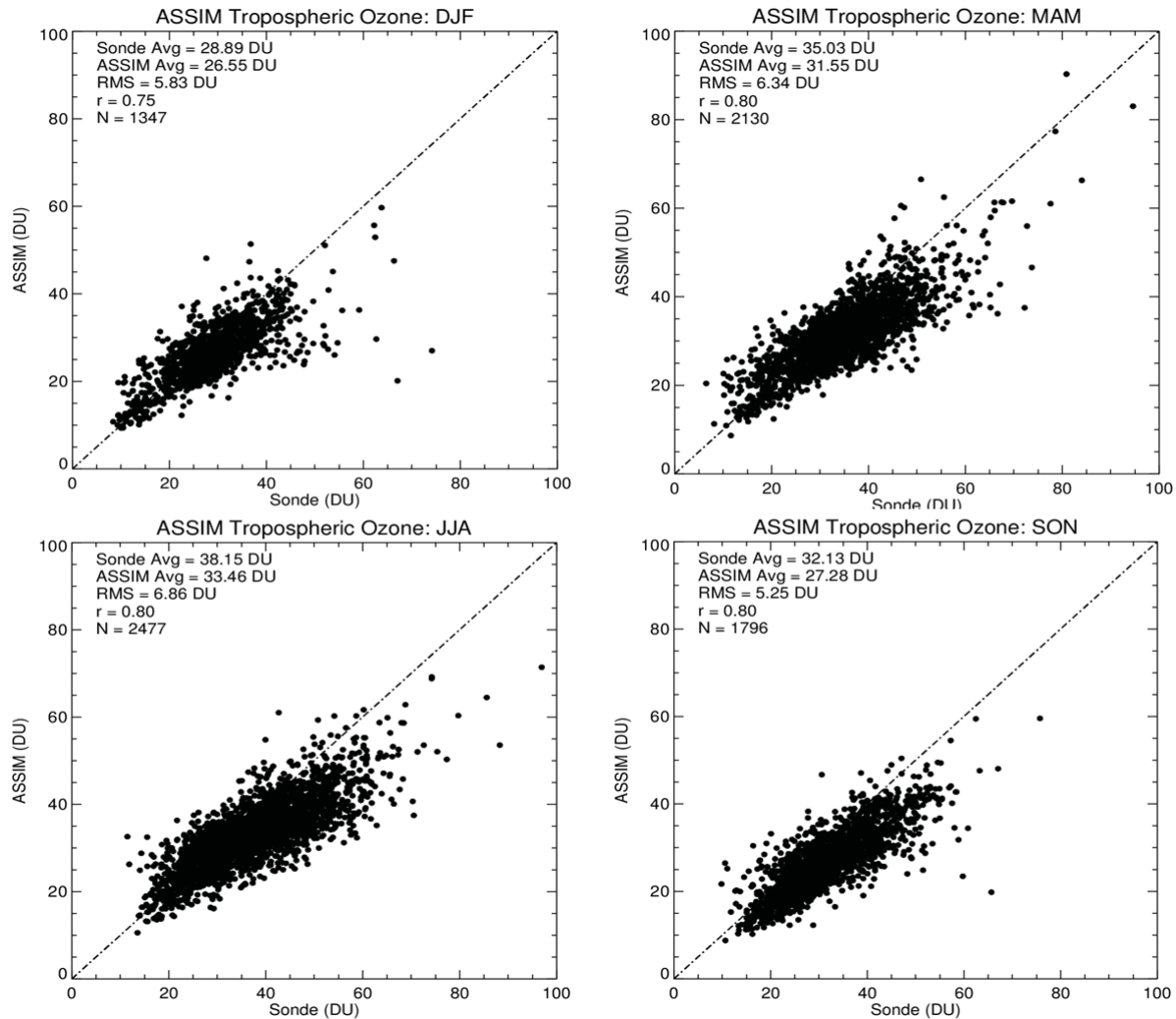
896

897

898 **Figure 3.** Expansion of the product/ozonesonde TCO comparisons of Figure 2 as function of
 899 latitude band. These latitude bands vary from 20° to 40° intervals as follows: 60°S-90°S, 40°S-
 900 60°S, 20°S-40°S, 20°S-20°N, 20°N-40°N, 40°N-60°N, and 60°N-90°N. The top, middle, and
 901 bottom panels show data product (or model) minus sonde difference, product/model minus
 902 ozonesonde difference RMS, and correlation between product/model and ozonesonde,
 903 respectively. Also listed in the bottom panel is “N” which represents the total number of
 904 ozonesonde profiles included in these calculations.

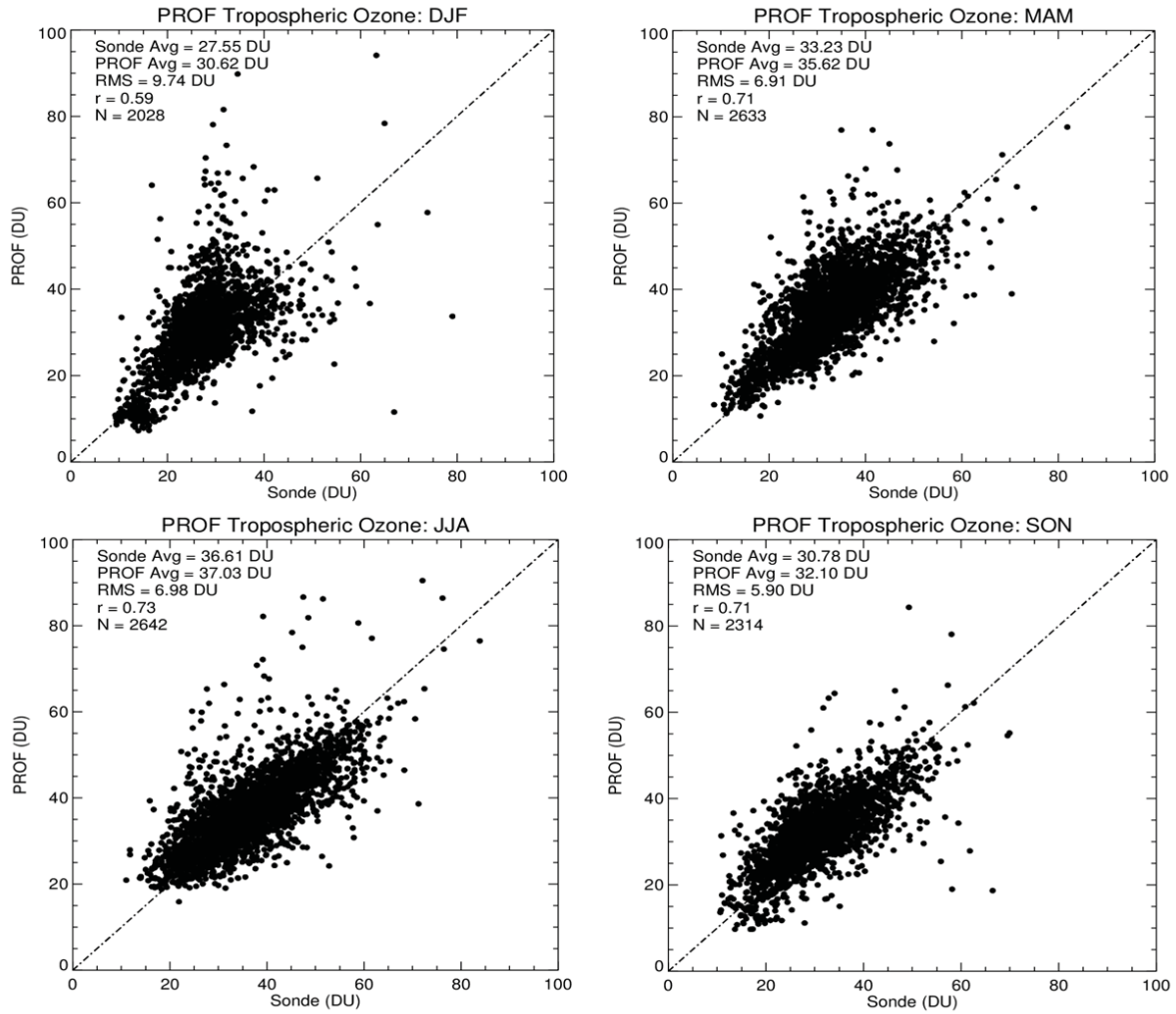
905

906



907

908 **Figure 4.** Daily TCO for GMAO data assimilation plotted versus coincident ozonesonde TCO
909 for the four 3-month seasons (indicated). Ozonesondes represent all available global station
910 locations. Included for each product in the scatter plots are their averages, difference RMS
911 value, correlation, and total number of data pairs. The 1-1 line is also shown. The years
912 included for ozonesonde comparisons for PROF are 2004-2008 and 2005-2010 for GMI, TRAJ,
913 and ASSIM.

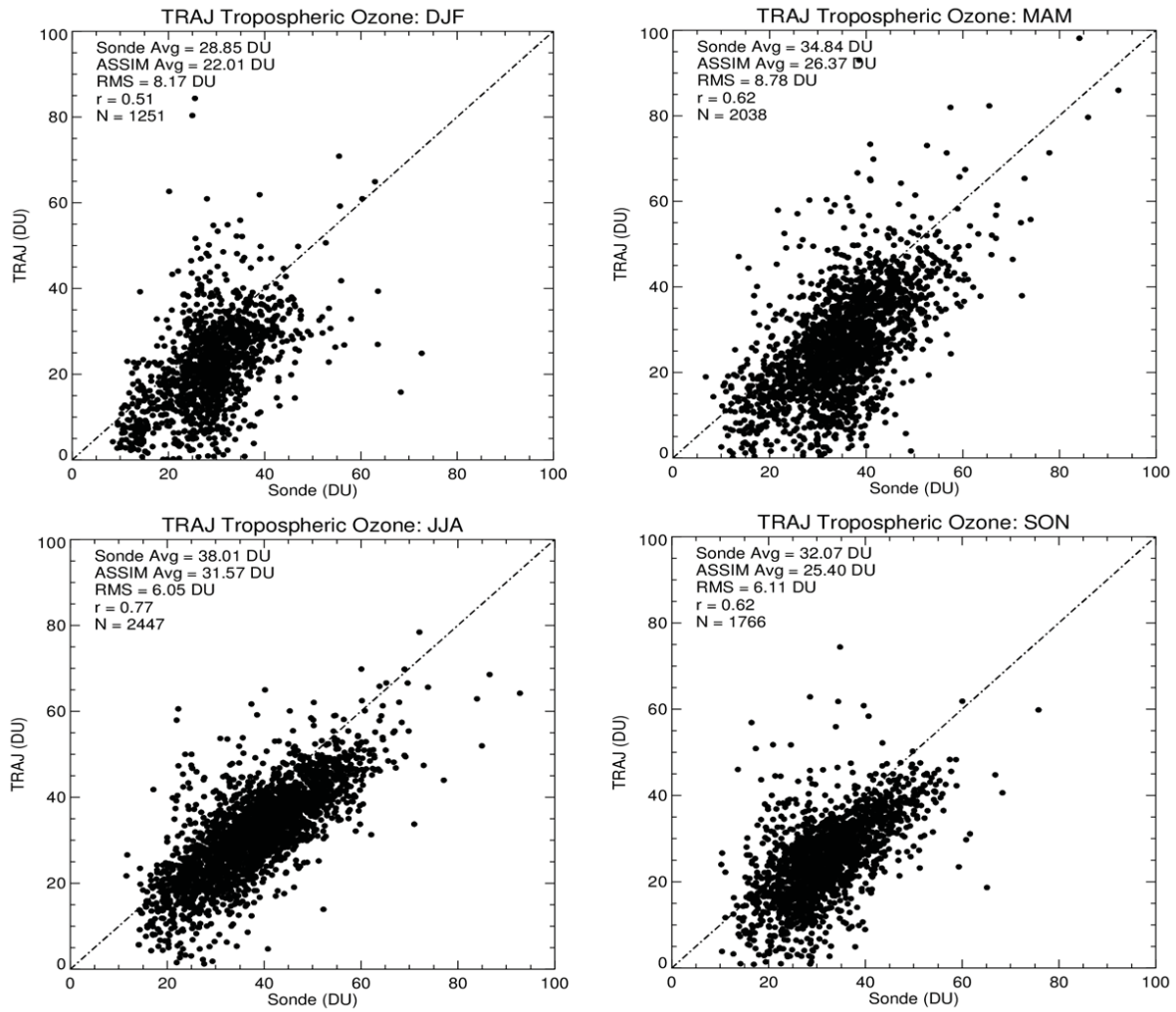


914

915 **Figure 5.** Same as Figure 4 but for direct profile retrieved TCO.

916

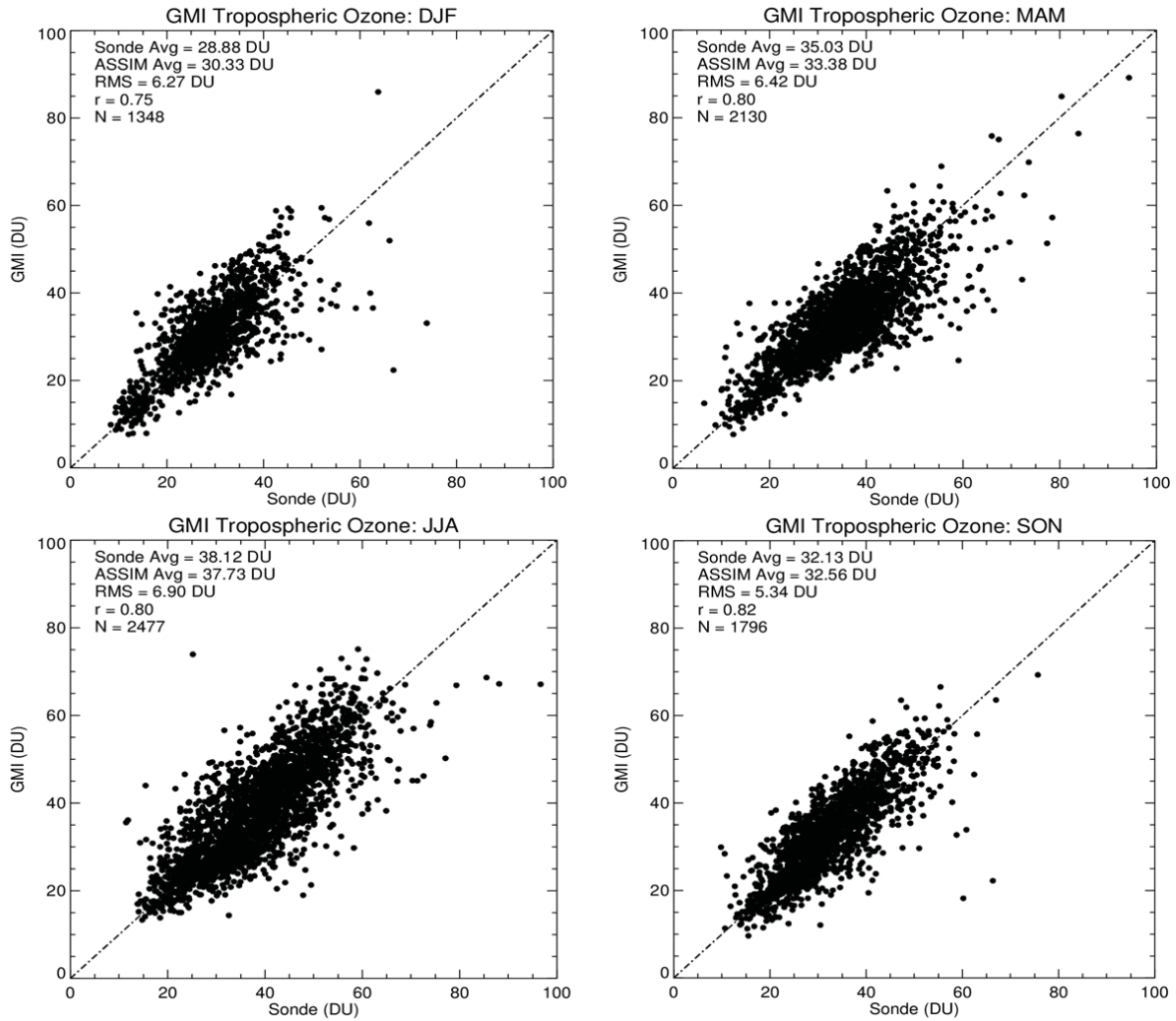
917



918

919 **Figure 6.** Same as Figure 4 but for trajectory mapped TCO.

920



921

922 **Figure 7.** Same as Figure 4 but for GMI model TCO.

923

924

925

926

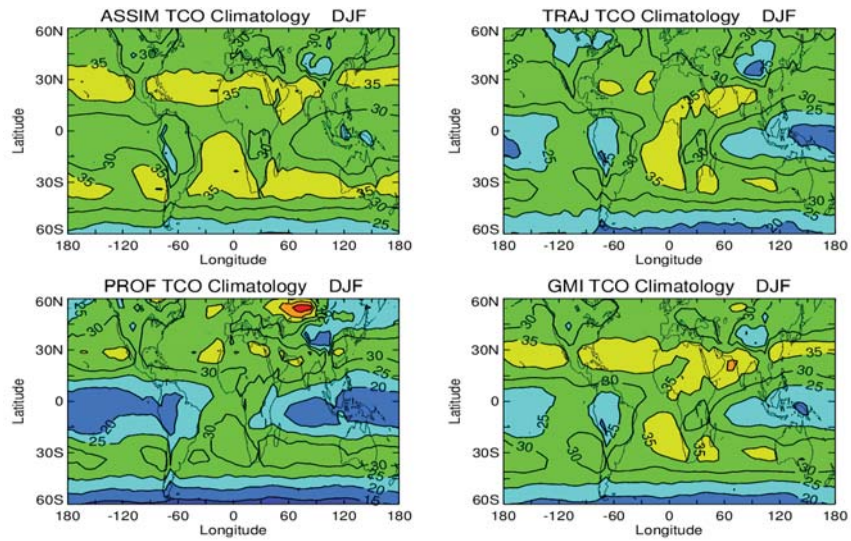
927

928

929

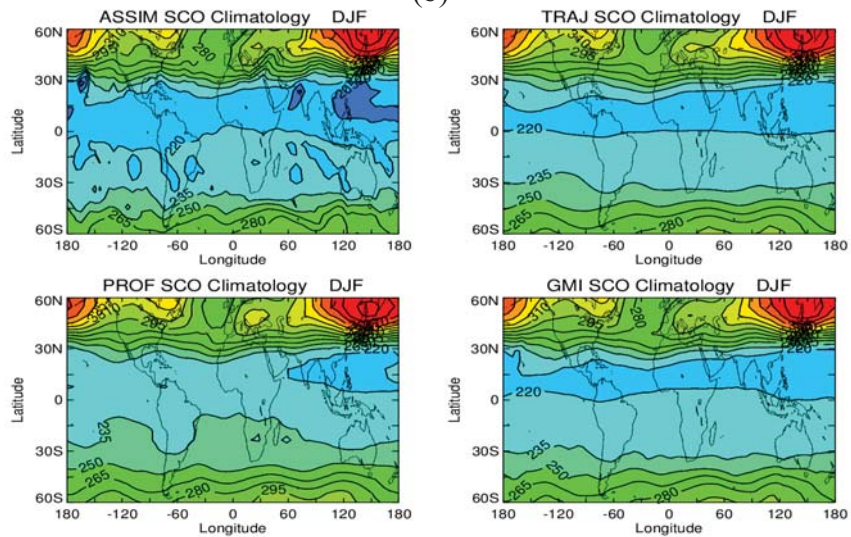
930
931
932

(a)



933
934

(b)



935
936
937
938
939
940
941
942
943

Figure 8. (a) Seasonal climatology of TCO (in Dobson Units) for the December-February season for each of the three products and GMI model (indicated). (b) Similar to (a) but for SCO. For this visualization comparison of spatial variability a constant offset of +4 DU, +7 DU, -2 DU, and 0 DU (based on ozonesonde differences in Figure 2) was applied to all TCO measurements for ASSIM, TRAJ, PROF, and GMI, respectively. These constant offsets were applied only for plotting TCO here and were not applied to the products in calculating the spatial statistics listed in Tables 1-3.

944

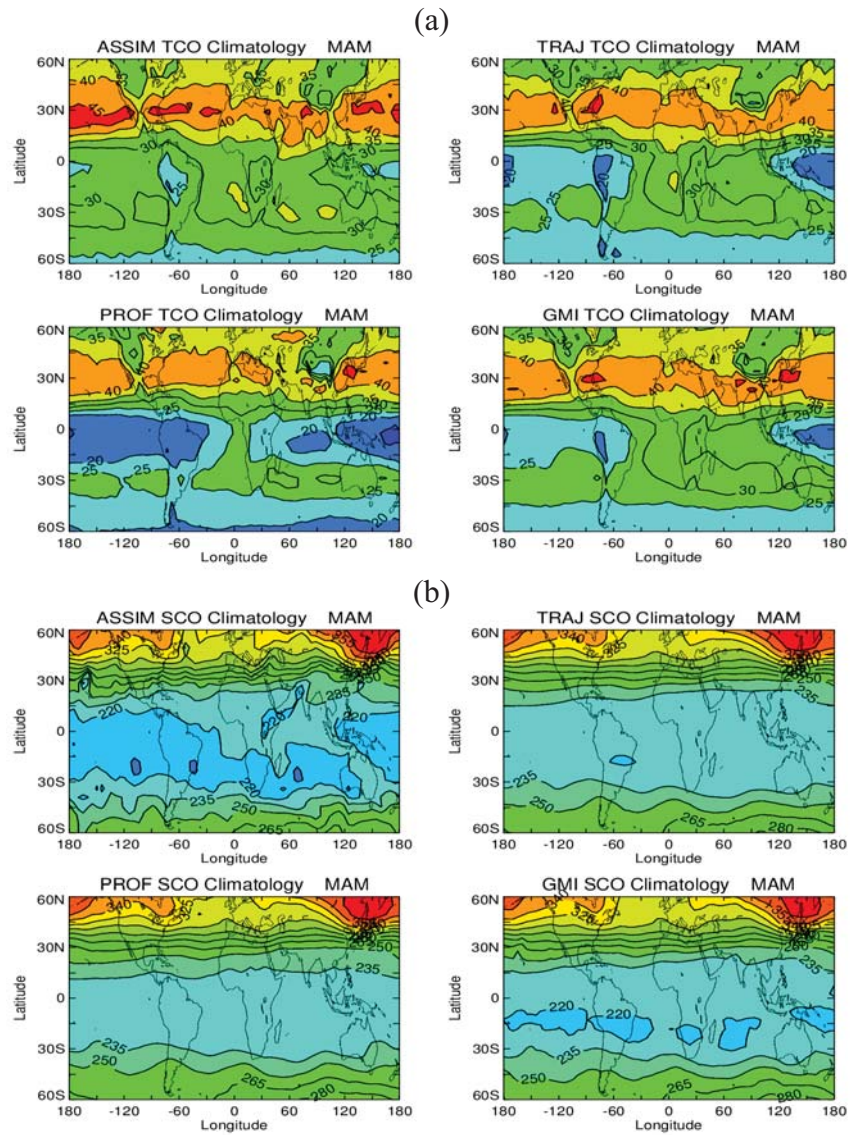
945

946

947

948

949



950

951

952

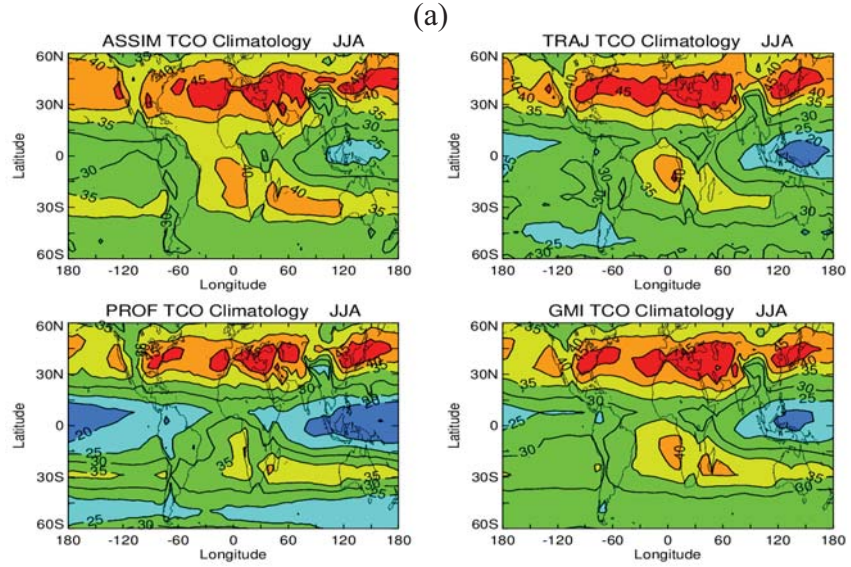
953

Figure 9. Similar to Figure 8 but instead for March-May season.

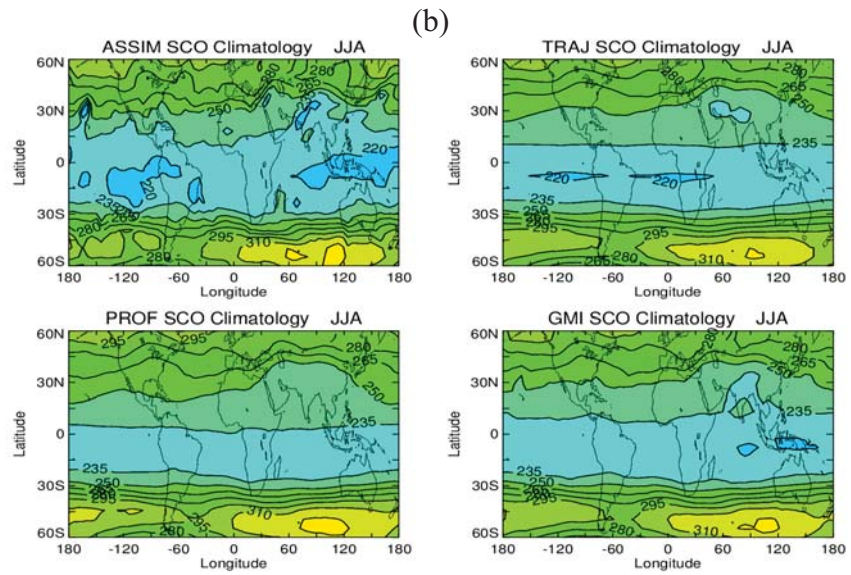
954

955

956



957
958



959
960

Figure 10. Similar to Figure 8 but instead for June-August season.

961

962

963

964

965

966

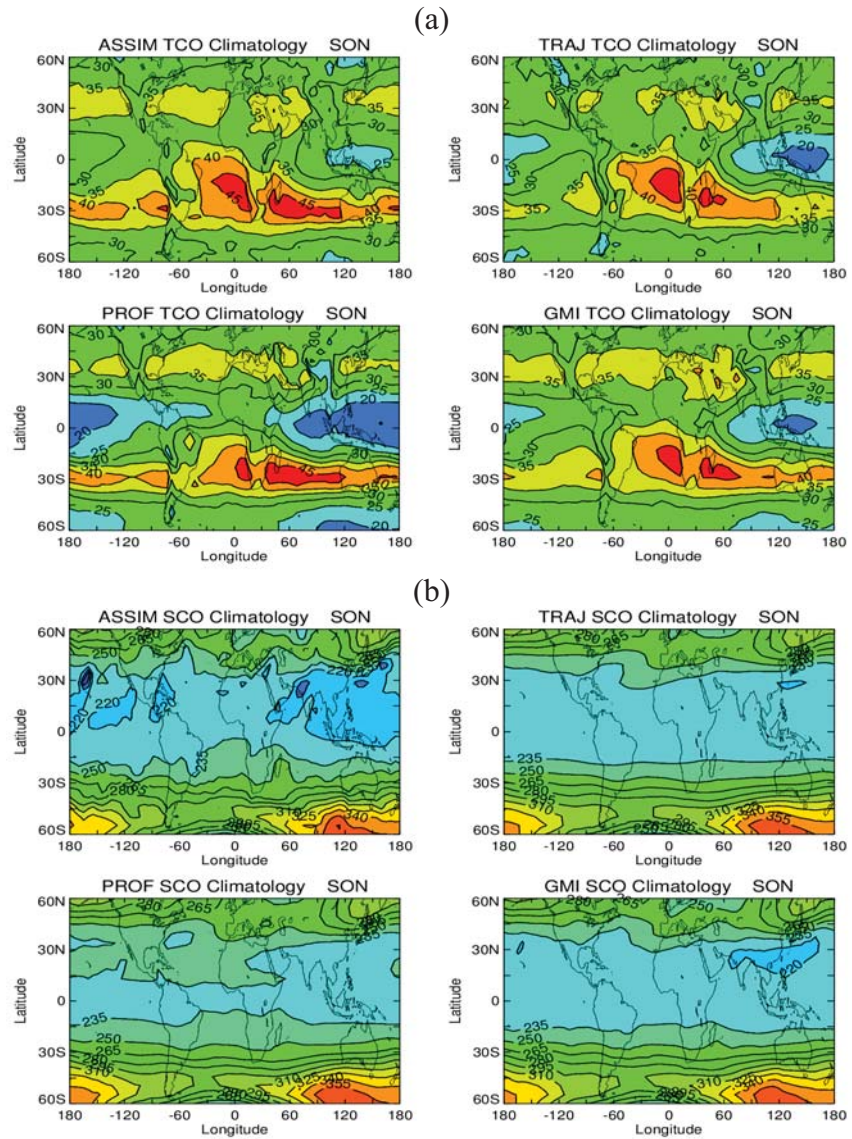
967

968

969

970

971



972

973

974

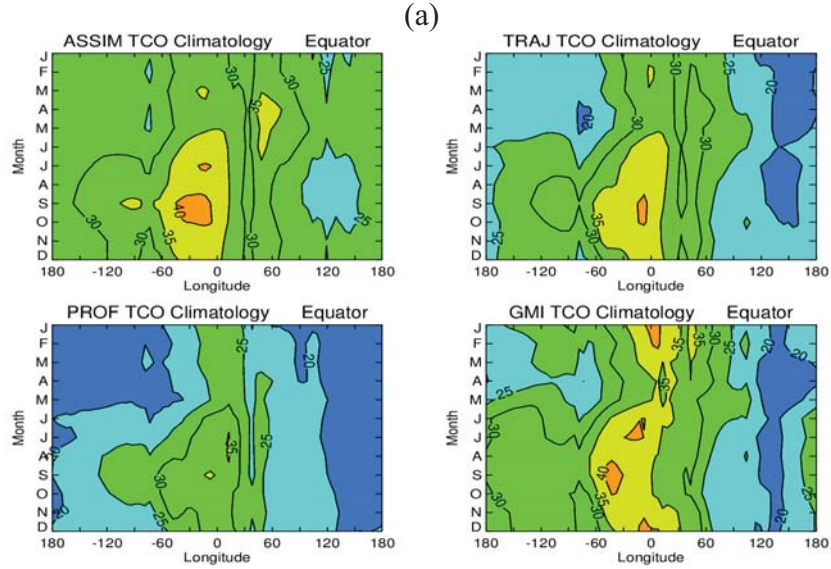
975 **Figure 11.** Similar to Figure 8 but instead for September-November season.

976

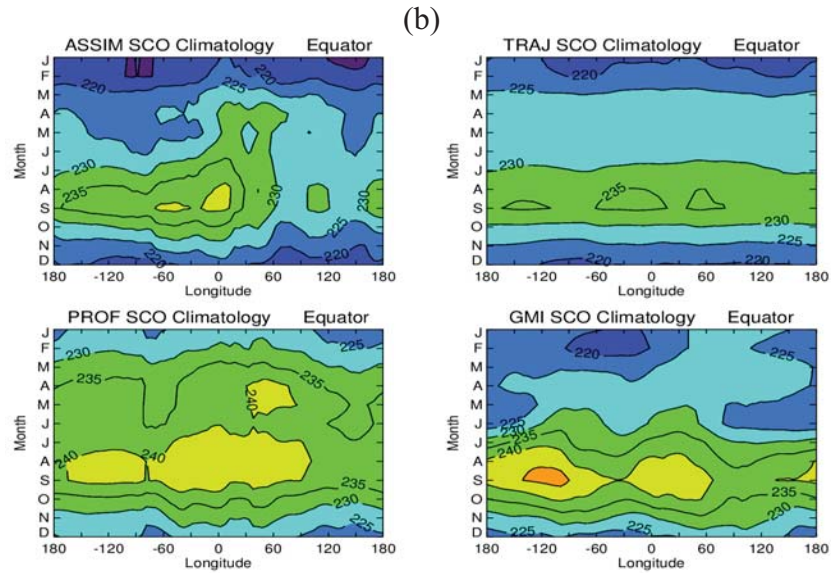
977

978

979



980
981



982

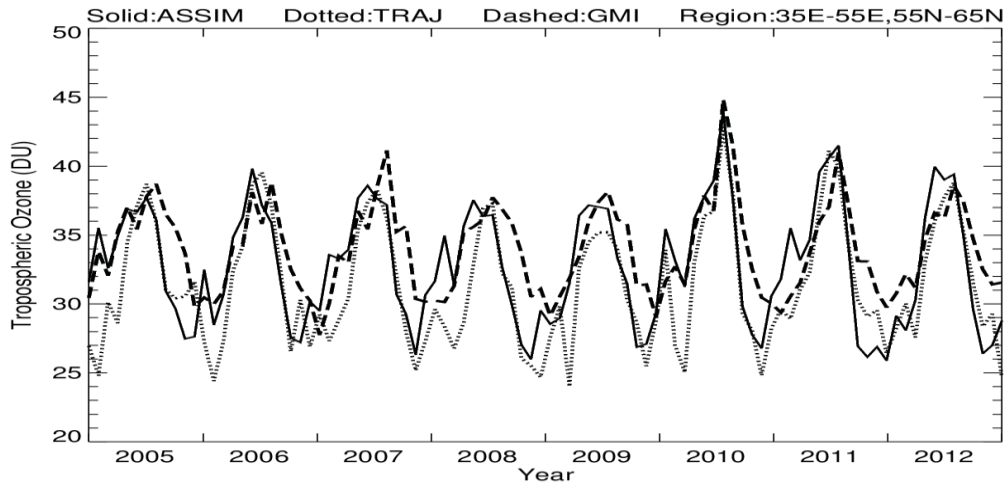
983 **Figure 12.** (a) Hovmoller plots of month versus longitude monthly TCO climatologies of the

984 three data products and GMI model along the equator. (b) Same as (a) but instead for SCO. All

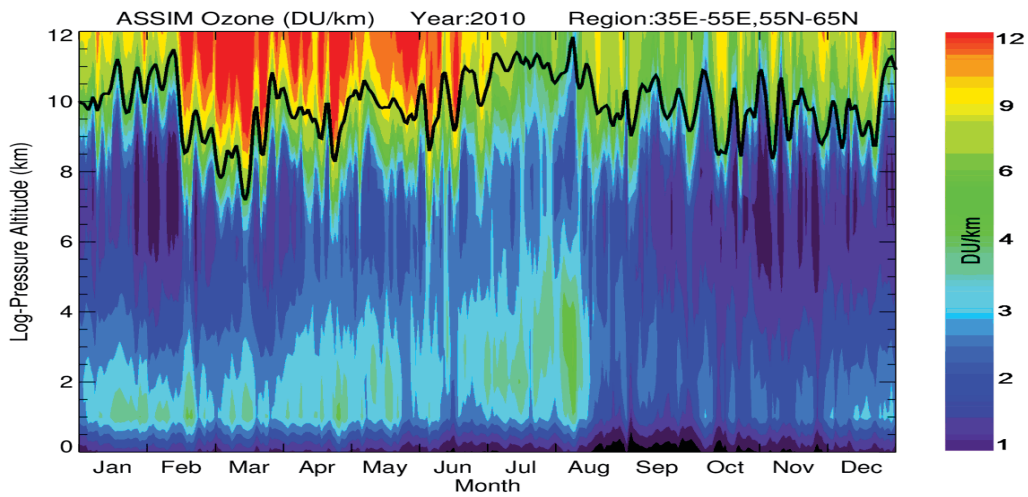
985 column amounts are in Dobson Units.

986

987



988

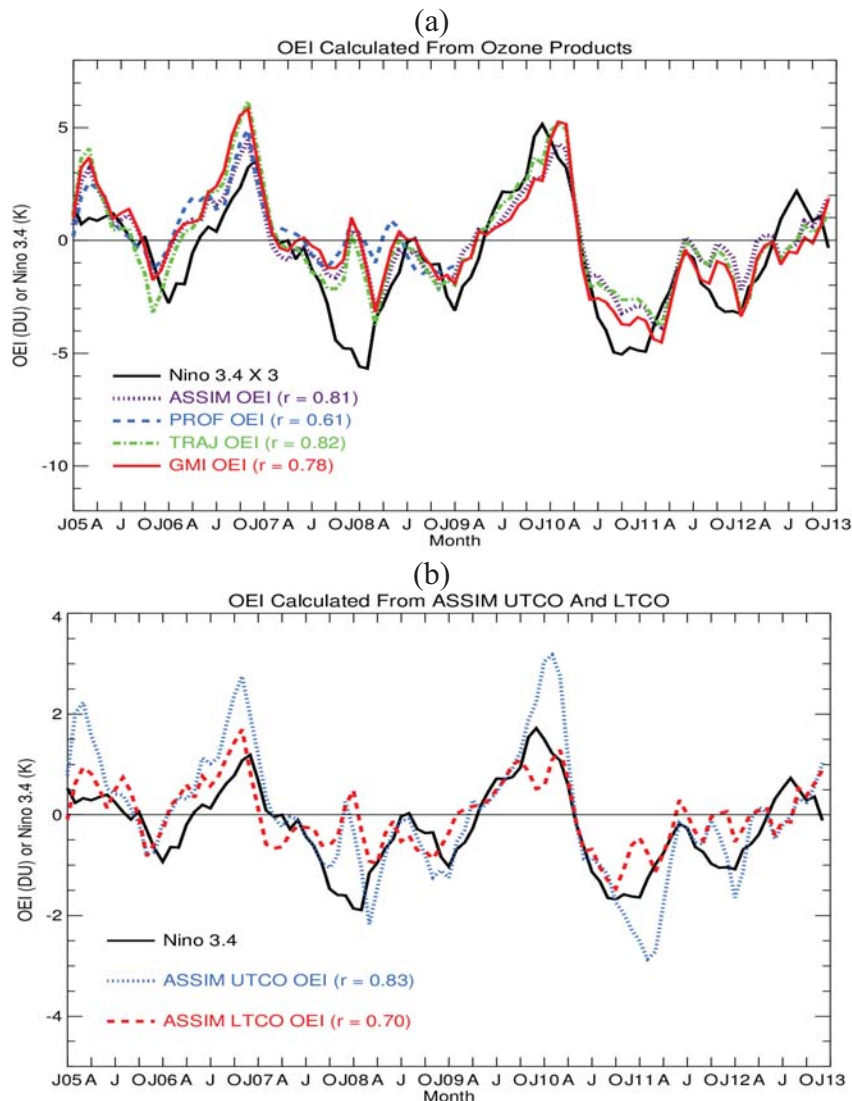


989

990 **Figure 13.** (top) Monthly mean TCO time series measurements averaged over western Russia
 991 from ASSIM (solid), TRAJ (dotted), and GMI model (long dashed). TCO for the three products
 992 was averaged over the region 35°E-55°E, 55°N-65°N. Anomalous increases in TCO over the
 993 region occurred in July 2010 for all three TCO time series in conjunction with record dry
 994 conditions involving high tropospheric temperatures and uncontrolled wildfires. (bottom)
 995 Contour plot of daily ozone profiles (calculated vertical gradients in DU-km⁻¹) from ASSIM for
 996 year 2010 over the same broad region. The thick black curve is NCEP tropopause pressure in
 997 log-pressure altitude.

998

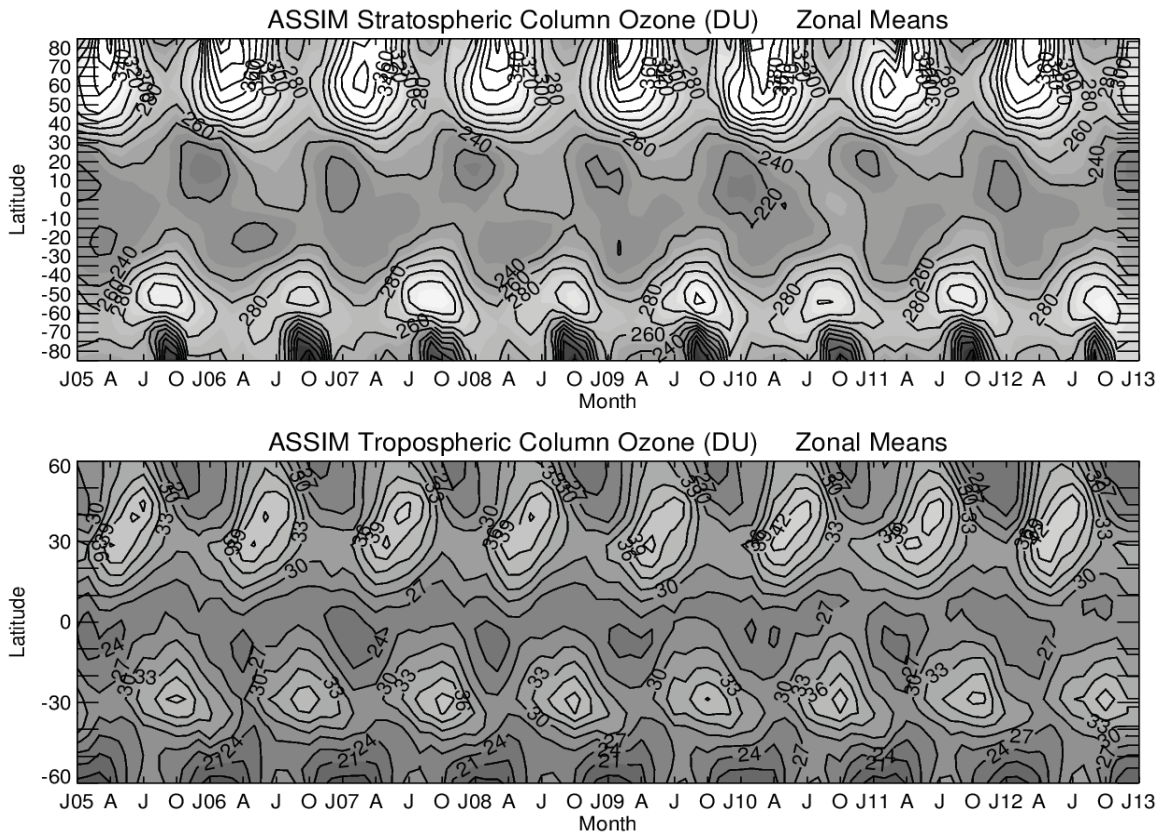
999



1000
1001

1002
1003

Figure 14. (a) Monthly tropospheric Ozone ENSO Index (OEI) derived separately from ASSIM (dotted purple curve), PROF (dashed blue curve), TRAJ (dotted-dashed green curve), and GMI (solid red curve). Also shown is the Niño 3.4 monthly temperature anomaly ENSO index (solid black curve) along with listed time series correlations “r” between the Niño 3.4 index and OEI’s from the three products and CTM. OEI time series are given in Dobson Units while the Niño 3.4 units are in K. All four OEI’s extend from January 2005 through December 2012 except for PROF OEI which ends December 2008. (b) ASSIM upper tropospheric column ozone (UTCO, dotted blue curve) is plotted with lower tropospheric column ozone (LTCO, dashed red curve) and Niño 3.4 (solid black curve). Upper and lower tropospheric column ozone are defined as the ozone column from 500 hPa to tropopause and 500 hPa to ground, respectively.



1013

1014 **Figure 15.** (top) Monthly zonal mean SCO in Dobson Units for 2005-2012 from the data
 1015 assimilation product. (bottom) Same as top panel but instead for TCO. Dark to light shading in
 1016 each panel designates smaller to higher column amounts, respectively. The contour values for
 1017 the top panel (bottom panel) increments by 20 (3) Dobson Units.

1018

1019

1020

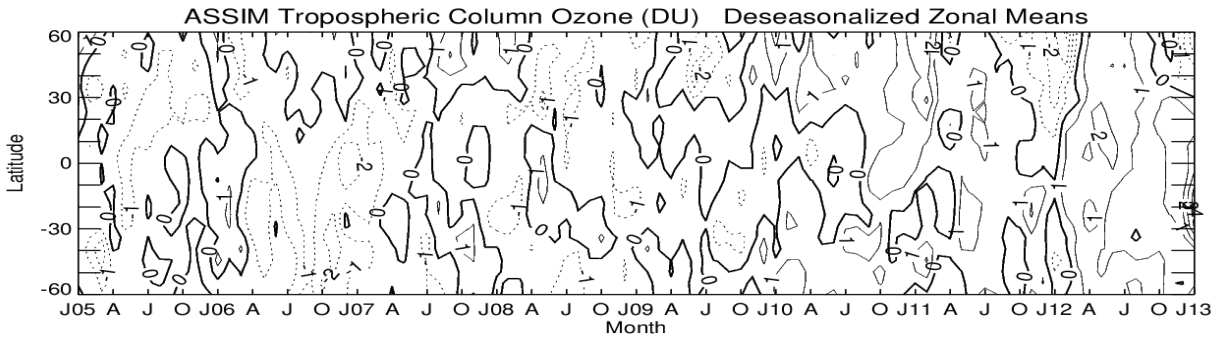
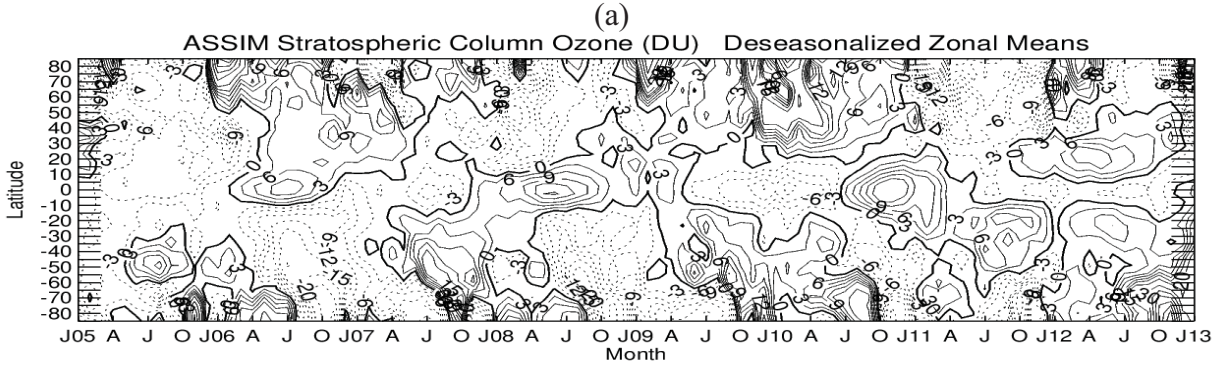
1021

1022

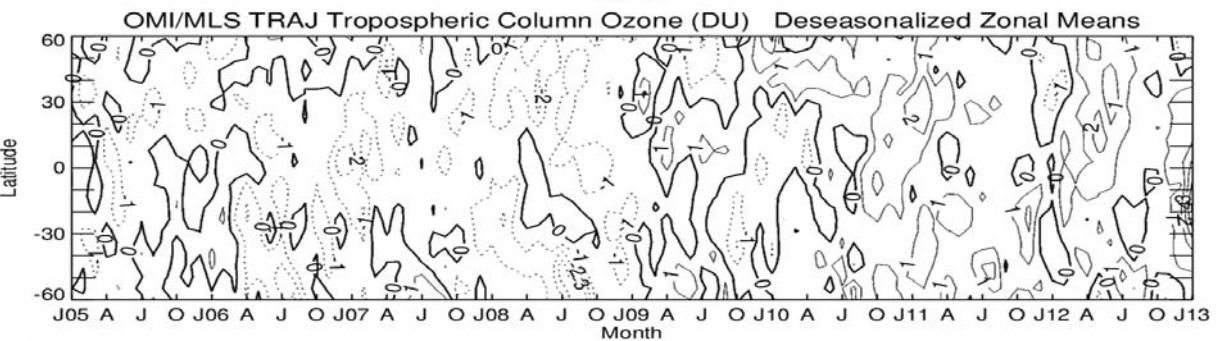
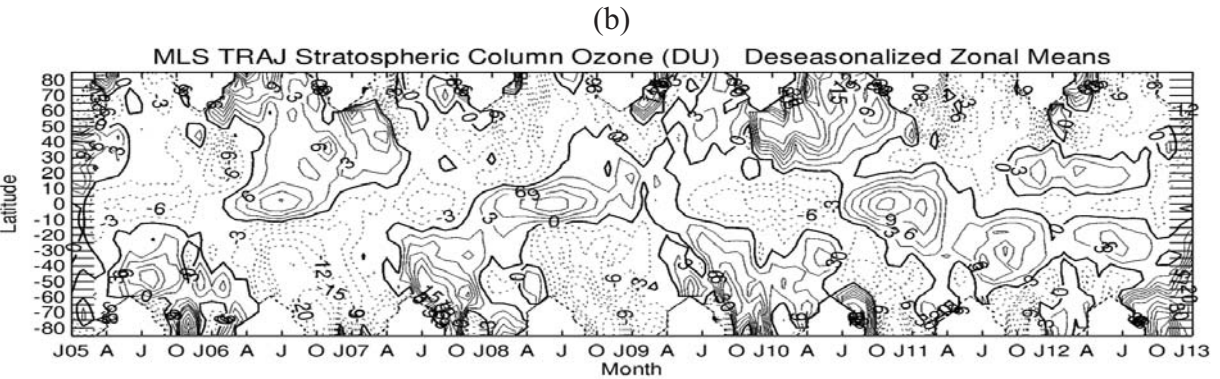
1023

1024

1025



1026
1027



1028
1029

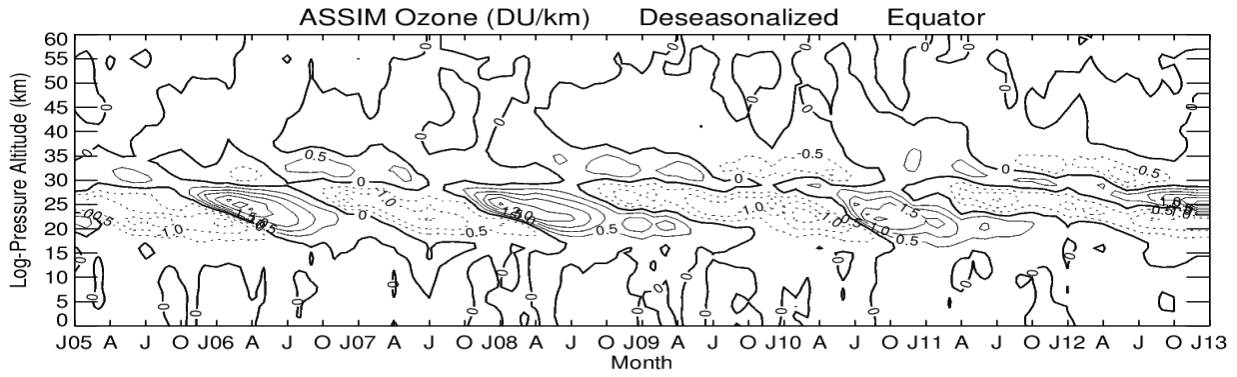
Figure 16. (a) Contour diagrams of the same ozone data plotted in Figure 15 but with all measurements deseasonalized. The contour increments for the top panel (bottom panel) is three (one) Dobson Units. (b) Same as (a), but instead for TRAJ SCO and TCO measurements.

1030
1031

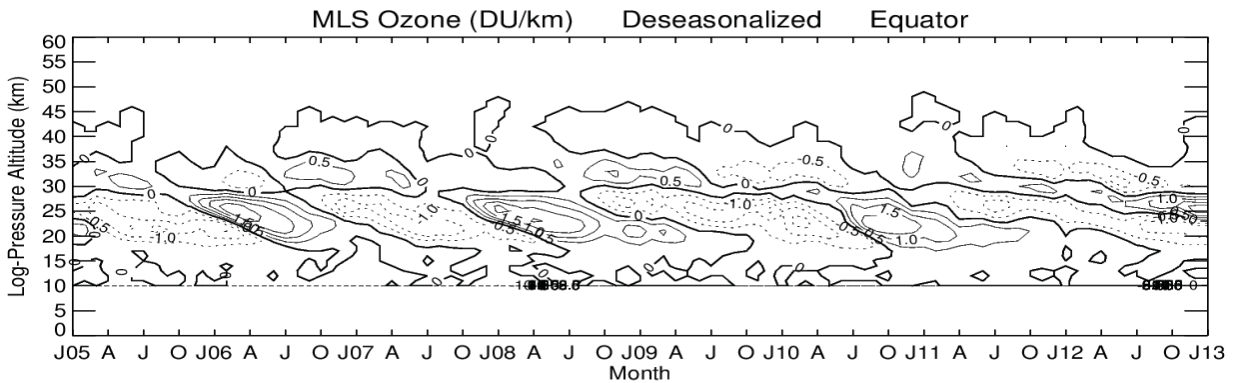
1032

1033

1034



1035



1036

1037 **Figure 17.** (top) Equatorial ozone vertical profile gradients (in units $\text{DU}\cdot\text{km}^{-1}$) from the data
1038 assimilation product plotted as log-pressure altitude (in units km) versus month. The vertical
1039 gradients are derived from monthly means by interpolating the product log-pressure surface
1040 ozone measurements to pressure levels $1013.25\cdot\exp(-z/7)$ where z is log-pressure altitude in units
1041 km and the pressure is in units hPa. (bottom) Same as (top) but for MLS ozone profiles.

1042

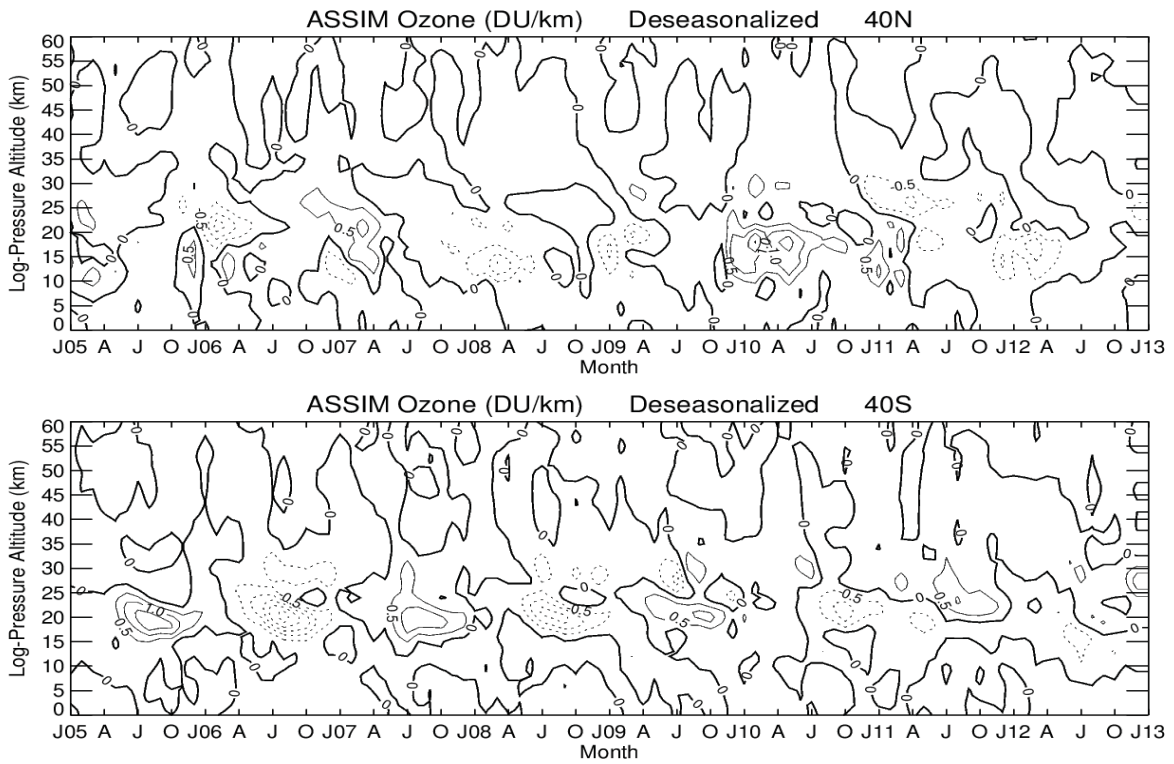
1043

1044

1045

1046

1047



1048

1049 **Figure 18.** (top) Same as Figure 17 for ASSIM ozone but instead at latitude 40°N. (bottom)

1050 Same as Figure 17 for ASSIM ozone but instead at latitude 40°S.

1051

1052

1053

1054

1055

1056

1057

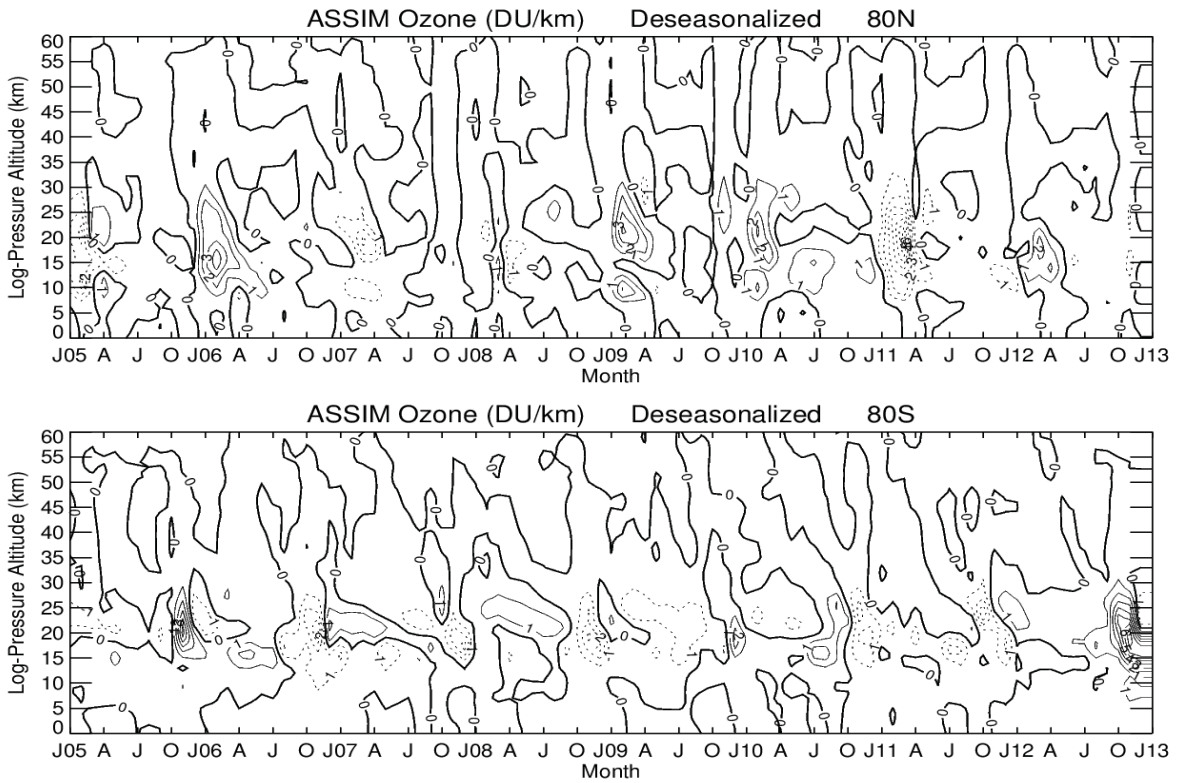
1058

1059

1060

1061

1062



1063

1064 **Figure 19.** (top) Same as Figure 17 for ASSIM ozone but instead at latitude 80°N. (bottom)

1065 Same as Figure 17 for ASSIM ozone but instead at latitude 80°S.

1066